Advancements in DSC and BOLD perfusion imaging

Acquisition, analysis and clinical application

Jonathan Arvidsson

Department of Medical Radiation Sciences
Institute of Clinical Sciences
Sahlgrenska Academy, University of Gothenburg

UNIVERSITY OF GOTHENBURG

Gothenburg 2023

Cover illustration: The capillary bed with a single input and output orifice,
imagined by Midjourney v5.2 and Jonathan Arvidsson
printed under the CC BY-NC 4.0 license

SVANENMÄRKET

Trycksak
3041 0234

Anicca

ABSTRACT

This thesis is focused on perfusion MRI techniques and topics related to image acquisition, analysis and clinical applications. The first half of the thesis is focused on dynamic susceptibility contrast (DSC) MRI, a technique which is based on the contrast enhancements caused by an intravenously administered paramagnetic contrast agent. The second half of this thesis is focused on blood oxygen level dependent (BOLD) MRI, which leverages a signal effect caused by paramagnetic properties of venous blood. For application in peripheral muscle, this signal effect can be enhanced by restricting the blood flow of a feeding artery to the studied tissue. In papers I and III, it is shown that the duration of the contrast agent injection and the duration of the flow restriction, indeed affects the measures of perfusion produced with these techniques.

The pathophysiology of normal pressure hydrocephalus (iNPH) is not completely understood, but symptoms point toward brain stem regions. In paper II, DSC-MRI and diffusion MRI was applied to patients with iNPH, pre and post shunt-surgery, showing the possible involvement of these regions in iNPH symptoms and disease reversibility.

In paper IV peripheral muscle BOLD was applied to patients with peripheral artery disease (PAD) and controls, in an exploratory study. Perfusion related measures derived from acquired BOLD curves were able to separate between PAD patients and controls, in accordance with previous studies. Further data exploration found a number of curve traits that could be indicative of potential disease phenotypes, and these have now been documented. As the technique continues to develop towards individual prognostication, these curve traits may be of value for establishing disease severity.

In conclusion, this work has made advancements of the common knowledge base within the field of perfusion imaging, spanning from the well-studied area of DSC-MRI to the comparatively new technique of peripheral muscle BOLD imaging and their application to clinically relevant patient cohorts.

POPULÄRVETENSKAPLIG SAMMANFATTNING

Som medicinsk utrustning är magnetkameran enastående. Den är känslig för variationer i magnetfält och rörelser på mikroskopisk nivå i kroppen och kan ge detaljerade bilder av anatomiska strukturer. Magnetkameran kan också göras känslig för olika egenskaper hos vävnaden, vilket möjliggör att bilden kan skräddarsys för specifika diagnostiska frågeställningar.

Flödet av blod genom kapillärbädden i en vävnad kallas för perfusion. Denna avhandling är inriktad på magnetkameratekniker för perfusionsavbildning samt frågeställningar kopplade till bildinsamling, perfusionsanalys, samt teknikens kliniska tillämpningar. Den första halvan av avhandlingen fokuserar på en teknik för perfusionsavbildning där blodflödes bildkontrast förstärks av ett intravenöst givet kontrastmedel (DSC-MRI). Avhandlingens andra halva är fokuserad på blodsyrenivåkänslig magnetkameraavbildning (BOLD-MRI), som utnyttjar en signaleffekt orsakad av magnetiska egenskaper hos venöst blod. Signaleffekten förstärks i den här tekniken genom att tillfälligt stoppa blodflödet till vävnaden i en matande artär. I artiklarna I och III visas att längden på kontrastmedelsinjektionen respektive flödesbegränsningen faktiskt påverkar de perfusionsmått som tas fram med teknikerna.

Den bakomliggande sjukdomsmekanismen vid idiopatisk normaltryckshydrocefalus är ännu inte helt klarlagd, men symtombilden pekar mot funktioner som kan kopplas till hjärnstammen. I artikel II applicerades DSC-MRI på patienter med idiopatisk normaltryckshydrocefalus, före och efter shuntkirurgi. Resultaten tyder på områdets sannolika inblandning i symptombilden, samt symptomförbättring efter shuntkirugi.

I artikel IV presenteras en explorativ studie, där BOLD-MRI i vadmuskel applicerades på patienter med perifer artärsjukdom och kontrollpersoner. I enlighet med tidigare studier visades att perfusionsberoende kurvegenskaper möjliggjorde en särskiljning mellan patienter och kontroller. Med ytterligare analyser kunde flera nya kurvegenskaper påvisas; egenskaper som eventuellt speglar sjukdom. När tekniken fortsätter att utvecklas mot individuell prognostisering kan de här egenskaperna vara av värde för fastställande av svårighetsgraden av perifer artärsjukdom.

Sammanfattningsvis har den här avhandlingen bidragit till kunskapen inom perfusionsavbildning med den välstuderade tekniken DSC-MRI samt den jämförelsevis nya tekniken BOLD-MRI i perifer muskel, samt teknikernas tillämpning inom kliniskt relevanta patientkohorter.

LIST OF PAPERS

This thesis is based on the following studies:

I. **Effects of bolus injection duration on perfusion estimates in dynamic CT and dynamic susceptibility contrast MRI**

    Jonathan Arvidsson, Göran Starck, Kerstin Lagerstrand, Doerthe Ziegelitz and Oscar Jalnefjord
    Magnetic Resonance Materials in Physics, Biology and Medicine 2022 36:95-106 DOI: 10.1007/s10334-022-01038-y

II. **MRI diffusion and perfusion alterations in the mesencephalon and pons as markers of disease and symptom reversibility in idiopathic normal pressure hydrocephalus**

    Simon Agerskov[*], **Jonathan Arvidsson**[*], Doerthe Ziegelitz, Kerstin Lagerstrand, Göran Starck, Isabella Björkman-Burtscher, Carsten Wikkelsö and Mats Tullberg
    PLOS ONE 2020 15(10):1-13
    DOI: 10.1371/journal.pone.0240327

III. **Arterial occlusion duration affects the cuff-induced hyperemic response in skeletal muscle BOLD perfusion imaging as shown in young healthy subjects**

    Jonathan Arvidsson[*], Stefanie Eriksson[*], Edvin Johansson and Kerstin Lagerstrand
    Magnetic Resonance Materials in Physics, Biology and Medicine 2023
    DOI: 10.1007/s10334-023-01105-y

IV. **Exploring the dynamics of ischemia and reactive hyperemia with skeletal muscle BOLD imaging in patients with peripheral artery disease, age matched controls and young healthy subjects**

    Jonathan Arvidsson, Stefanie Eriksson, Oscar Jalnefjord, Edvin Johansson, Joakim Nordanstig and Kerstin Lagerstrand
    Manuscript

---

[*] Authors contributed equally

LIST OF CONTRIBUTIONS

Paper I

I participated in conceptualizing the study. I performed the experimental and the simulation-based perfusion evaluations and the statistical analysis. I was the main author of the manuscript.

Paper II

I contributed to the study design, implemented the perfusion estimation method and was responsible for the technique-related aspects of the manuscript, specifically data post-processing, perfusion, and diffusion parameter estimation. I shared the main authorship of the manuscript with the first author.

Paper III

I contributed to the study design. I participated in MRI data acquisition, and performed the perfusion data processing and the statistical analysis. I shared the main authorship of the manuscript with the second author.

Paper IV

I conceived the study design which was based mainly on previously acquired data. I participated in MRI data acquisition. I performed the data processing and the statistical analysis. I was the main author of the manuscript.

RELATED PRESENTATIONS

The following presentations are related to the studies of this thesis:

1. **BOLD MRI Perfusion in Peripheral Skeletal Muscle: Revealing the cuffing duration dependency**
   Stefanie Eriksson, **Jonathan Arvidsson**, Suhela Abubakar Mohammad, Edvin Johansson and Kerstin Lagerstrand
   Joint annual meeting ISMRM-ESMRMB 2022, London

2. **Can bolus injection duration explain the difference in CBF estimates from DSC- and CT-perfusion?**
   Jonathan Arvidsson, Oscar Jalnefjord, Göran Starck and Kerstin Lagerstrand
   ESMRMB Congress 2019, Rotterdam

3. **Regularized k-means clustering for segmentation of brain tissues using hemodynamic features in DSC-MRI**
   Jonathan Arvidsson, Oscar Jalnefjord, Fredrik Kahl and Göran Starck
   Joint annual meeting ISMRM-ESMRMB 2018, Paris

ABBREVIATIONS

ADC   Apparent Diffusion Coefficient
ASL   Arterial Spin Labelling
AIF   Arterial Input Function
BBB   Blood Brain Barrier
BOLD   Blood Oxygen Level Dependent
CBF   Cerebral Blood Flow
CBV   Cerebral Blood Volume
CEST   Chemical Exchange Saturation Transfer
DCE   Dynamic Contrast Enhanced
dMRI   Diffusion MRI
DSC   Dynamic Susceptibility Contrast
EPI   Echo Planar Imaging
fMRI   Functional MRI
Hb   Hemoglobin
iNPH   idiopathic Normal Pressure Hydrocephalus
IVIM   Intravoxel Incoherent Motion
MRI   Magnetic Resonance Imaging
MRS   MR Spectroscopy
MTT   Mean Transit Time
PAD   Peripheral Artery Disease
PASL   Pulsed ASL
RBC   Red Blood Cell
rCBF   relative Cerebral Blood Flow
ROI   Region Of Interest
SVD   Singular Value Decomposition
TE   Echo Time

CONTENTS

INTRODUCTION

Within medical imaging, most are familiar with structural imaging where the basis for diagnosis is the morphology of an object. Functional imaging extends beyond this and seeks to quantify physiological processes.

The last few decades have seen considerable research effort within magnetic resonance imaging (MRI) towards the development of quantitative mapping techniques. Measures of interest span from MR-related properties such as proton density and relaxation times to the mapping of concentrations of metabolites[1]. Even dynamic physiological processes such as the diffusion of water molecules, brain activation, and the supply of blood to tissues of the body have also been studied extensively within the field of quantitative MRI[1].

The term perfusion is used to denote the process of blood flowing through the microvasculature of a tissue (Fig. 1), a process critical for maintaining tissue viability[2]. The Within the microvasculature, capillaries serve as the main point of exchange for oxygen and nutrients to the cells and metabolic by-products such as carbon di-oxide away from the tissue[2]. Insights into this physiological process are thus important for in vivo assessments of organs involved in diseases where the symptoms include disturbances in tissue metabolism and cardiovascular function.
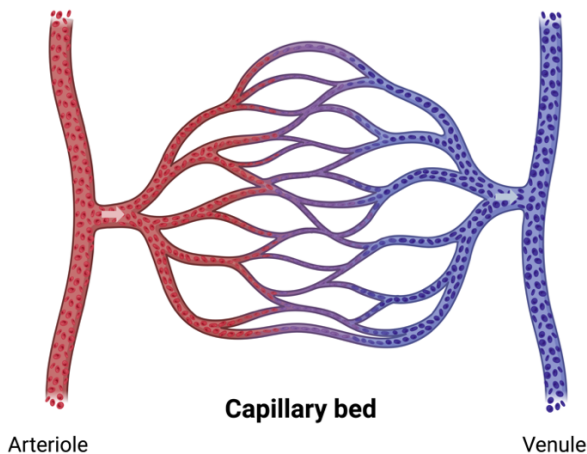

Figure 1. *Illustration of microvasculature with arterioles, venules, capillaries, and erythrocytes that are color coded to reflect the degree of oxygenation.*

Measuring perfusion has proven to be a difficult task and the clinical adoption of recent research developments has been relatively slow. While MR perfusion-related measures are presently used in the clinic, via contrast enhanced MRI and arterial spin labelling techniques, quantitative imaging-based perfusion parameters used clinically are not always achievable, one such example being dynamic susceptibility contrast MRI (DSC-MRI) in which normalized measures are used (rather than estimates on a ratio or interval scale[3]). While several technical challenges remain in order to leverage the full potential of perfusion imaging techniques, clinical adoption also depends on practical developments in which standardisation of acquisition, post-processing, and presentation schemes play important roles.

The topics of this thesis span from aspects of perfusion image acquisition and data analysis to the application of perfusion imaging in clinical subject cohorts. It also spans two different perfusion MRI techniques, one well established, for use in neurological perfusion imaging, DSC-MRI, and one novel candidate technique for use in the assessment of peripheral muscle, cuff-based blood oxygenation level dependant MRI (BOLD-MRI). The techniques differ substantially in how image contrast, to probe tissue perfusion, is created. DSC-MRI is dependent on the use of an exogenous contrast agent, administered via an intravenous injection. The contrast mechanism in cuff-based peripheral muscle BOLD-MRI leverages differences in the magnetic properties of arterial and venous blood and enhances these by first limiting, and subsequently releasing, the flow of blood to the tissue of interest. While DSC-MRI has been extensively researched over the last three decades and is routinely used in the clinic, cuff-based peripheral muscle BOLD imaging is still under technical development.

PHYSIOLOGICAL BACKGROUND

MICROCIRCULATION

The microcirculation includes the arterioles, venules, the capillary bed as well as the terminal lymphatic vessels. Together they make up a fine mesh of vessels embedded in almost every tissue of the body[2]. The primary function of the microcirculation is to adjust the blood flow according to the nutritional needs of the tissue and to transport away metabolic byproducts[2].

Arterioles are the smallest arteries that intersect with the capillary bed and have an average diameter of 30 μm or less[4]. The venule is the smallest draining vein with diameters varying from 8-100 μm[4]. The capillaries are the smallest blood vessels at only 5-10 μm in diameter and the primary point of exchange between tissue cells and the vascular system[4]. The diameter of the red blood cell (RBC) is about 7-8 μm[4], close to or even slightly larger than the capillary diameter[5], enforcing cell deformation during capillary flow. To allow for exchange between the vasculature and the cells, capillaries generally have leaky vessel walls. However, several different types of capillaries exist to support the specific needs of different organs. For example, the capillaries of the liver are highly permeable to allow proteins and cells to leave the vasculature[4]. In contrast, capillaries of the brain have an extremely low permeability and play an important role in maintaining the protective blood brain barrier (BBB)[4].

The arterioles play a major role in maintaining blood pressure and to keep a steady flow of blood through the microvasculature. As the blood enters the capillaries, the RBC velocity decreases from ~5-10 mm/s to ~1 mm/s[6]. This is in stark contrast to the RBC velocity of ~300 mm/s as found in larger arteries[4]. However, the velocity of blood through individual capillaries is not precisely constant. Rather, it follows oscillating flow pattern dictated by chemical signaling in response to the present tissue environment. At the inlet to each capillary, pre-capillary sphincters control the flow of blood to the vessel and different combinations in the level of hydrogen ion, lactic acid, tissue oxygen and carbon dioxide will either cause a vasodilation or vasocontraction, effectively increasing or decreasing capillary exchange[4].

According to the Fåhraeus effect, the volume percentage of RBCs in blood is lower in capillaries than in larger vessels[7]. Partly, this is due to the RBCs distribution in the axial center of small vessels (diameter < 30 µm), but also to the laminar flow, where RBCs move faster than the outer layer of plasma (and the average blood velocity). When tracer kinetic modeling is used as the basis for analyses to derive perfusion estimates on an absolute scale, corrections for differences in arterial and capillary hematocrit, the ratio of RBC to whole blood volume, is thus necessary.

The convention for reporting perfusion parameters has been to relate the intravascular volume and flow to a reference tissue mass of 100g, yielding units ml/100g tissue and ml/min/100g, for blood volume and blood flow, respectively. The reference tissue mass is used to enable the comparison of perfusion estimates regardless of organ size. An alternative formulism also used, is the reporting of perfusion levels in relation to a reference volume of 100 ml tissue, this is also recommended in a recent perfusion reporting lexicon under development by the open science initiative for perfusion imaging (OSIPI)[8] initiated by the perfusion study group of the international society for magnetic resonance in medicine (ISMRM).

Table 1. *Neurological reference measures of perfusion, cerebral blood flow (CBF), cerebral blood volume (CBV) and mean transit time (MTT) in gray and white matter [9] and peak blood flow measured in peripheral muscle of peripheral artery disease (PAD) patients and controls [10]*

Perfusion measure	Healthy subjects		Patients
Neurological measures	Gray matter	White matter	-
CBF (ml/min/100ml)	35-60	17-28	
CBV (ml/100ml)	3.5-6.6	2.1-3.0	-
MTT (s)	3.8-6.6	4.6-7.4	
Peripheral muscle	Anterior tibialis		PAD
F_{peak} (ml/min/100g)	80 ± 23		48 ± 16

Perfusion measures can be achieved on an absolute scale in accordance with the tracer kinetic theory as shown in Table 1. for brain and peripheral muscle tissue, and as presented in the following chapters. However, in practical imaging scenarios, a number of challenges make absolute quantification less feasible in everyday clinical use. Clinical implementations of DSC-MRI are, for example, typically confined to relative measures of perfusion. In this thesis, the results of paper I bear relevance for quantitative perfusion imaging. In paper II, relative estimates of perfusion were derived. In paper III and IV signal

representation-based, rather than model-based analyses of perfusion were derived.

PATHOLOGY AND CLINICAL FEATURES

Microvascular disease and dysfunction are terms used for a broad set of conditions[11]. Severe microvascular pathologies include abnormal tumor vasculatures and arteriovenous malformations, as illustrated in Fig. 2[12]. Abnormal tumor vasculature, driven by tumor angiogenesis, is often highly perfused with vessel leakage[13]. Arteriovenous malformations are characterized by tangles of macrovascular vessels that allow high-flow arteriovenous communication without passing through the capillary bed[14]. These examples illustrate somewhat extreme cases of microvascular abnormities. In many diseases, perfusion disturbances are closer to the normal variation, which thus require sensitive and specific perfusion measurement techniques.
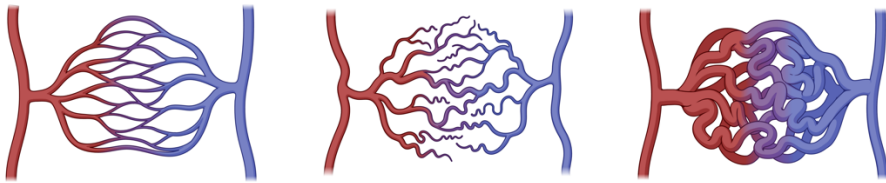

Figure 2. Illustrations of capillary beds found in healthy tissue, abnormal tumor vasculature, and arteriovenous malformations.

iNPH

In addition to volumetric increases in the lateral ventricles of the brain, late-onset idiopathic normal pressure hydrocephalus (iNPH) is combined with a set of clinical symptoms: impaired gait and posture, cerebellar T_2^*-time curves and paratonia, impaired wakefulness and urinary incontinence. The pathophysiology is not fully understood, but there is clear association with cardiovascular disease, mainly hypertension and diabetes mellitus[15–17]. Increased prevalence of white matter lesions has also been found in iNPH patients[17].

The clinical relevance of radiological assessments is motivated both by the clinical need to qualify patients for surgical interventions, but also to gain better understanding of the disease manifestation and development. While many patients are too fragile for surgery, a number of patients that are accepted for surgery do not improve. Being able to separate these non-responders from responders prior to surgery is an important topic of research towards increased

efficiency of clinical treatments for iNPH patients. The involvement of vascular risk factors and the fact that postoperative increases in perfusion of periventricular regions have been shown[18], indicate that perfusion is relevant to study within this patient group.

PAD

Peripheral artery disease (PAD) is a category of vascular disease in which the flow of blood in peripheral arteries, typically in the lower limbs, is limited due to obstructions or vascular stiffening. Causes of the disease include increasing age, hypertension, tobacco use, diabetes, and hypercholesterolemia[19]. The symptoms range from intermittent ischemic-related pain (claudication) to critical limb ischemia with pain at rest and/or ulcers[20]. PAD is often accompanied by loss of muscle mass, sarcopenia, and degradation of muscle strength. The mechanics between sarcopenia and PAD remain to be established, but findings show likely involvement of oxidative stress, inflammation, mitochondrial dysfunction, and enhanced protein degradation as well as impaired muscle regeneration[20].

As critical limb ischemia becomes severe, wound healing in the peripheral body regions is impaired, to the extent that surgical interventions cannot be advised. For this subgroup of patients, even revascularizing surgery must be considered with care. Image-based measures of perfusion may provide additional information with the potential to aid the diagnostic question of whether a patient can benefit from surgical interventions or not.

PERFUSION IMAGING

Several medical imaging modalities have been utilized to capture perfusion in vivo including positron emission tomography (PET), single photon emission computed tomography (SPECT), Doppler ultrasound, dynamic contrast enhanced computed tomography (DCE-CT) and MRI[21]. The most common strategy is to leverage the signal dynamics produced by the injection of an intravascular contrast agent. However, particularly within MRI there are alternative contrast mechanisms available such as arterial spin labelling (ASL) and BOLD. Each of these techniques provides unique image contrasts and prerequisites for the quantification of perfusion.

BIOPHYSICAL MODELS AND SIGNAL REPRESENTATIONS

According to Novikov et al.[22], a majority of quantification techniques within diffusion MRI (dMRI) falls within one of two broad categories referred to as *biophysical models* and *signal representations*. This nomenclature also bears relevance to the field of perfusion MRI in general, but also in this thesis, as the analyses in DSC-MRI and cuff-based BOLD-MRI fall into different categories. While the analysis of DSC-MRI is based on tracer kinetic theory and a model of the vascular bed, the cuff-based BOLD MRI technique is based on a signal representation.

Biophysical models require an underlying theory to interpret the measurements of an observed phenomenon. If the theory can be condensed and summarized into a parameterized mathematical expression, where each parameter holds specific biophysical meaning, it can be termed a biophysical model[23]. Parameter estimates of such an analysis can, if successful, provide *specific* insights to properties of the underlying physiology[23].

Signal representation is more straight forward in the sense that it simply conveys the fitting of a mathematical expression that can represent the data efficiently[23]. Such an analysis does not require any biophysical interpretation, and the parameters of the fitted expression will typically not carry a specific biophysical meaning. Analyses building on signal representations are often combined with a second step, where measures such as amplitudes, slopes, and durations are derived from the fitted representation. Although less specific,

representative analyses can provide measures that are *sensitive* to the observed biophysical phenomena and thus still provide valuable insights in clinical settings.

To differentiate between the measures that these two analysis strategies produce, this thesis has used the term "*perfusion parameters",* for parameters of model-based analyses and the term "*perfusion related measures"* for measures obtained via signal representation-based analyses.

DSC-MRI

DSC-MRI is typically used in neuro-imaging applications where the brain is assumed to have an intact blood brain barrier, hence where the contrast agent remains intravascular. In the following sections theory, underlying the perfusion analyses in paper I and II are presented. While original articles have been referred to, more recent publications have revisited and presented this theory[24–28].

Susceptibility contrast

In dynamic susceptibility contrast-based MRI, the measured signal is made sensitive to the presence of an intravascular paramagnetic contrast agent. In the presence of a static magnetic field, such as the B_0-field of the MR-system, the contrast agent, causes magnetic field inhomogeneities that alter the spins of nearby water molecules[29]. This effect spans the vasculature and extends some length into the extravascular space. On a macroscopic level, spatial variations in resonance frequencies of water molecules can be observed as a phase dispersion of the bulk magnetization, and a decrease in the MR signal magnitude, as registered by the MR-system[29].

Imaging sequence

Disregarding diffusion effects, the rephasing of altered spins to regain the signal magnitude and phase is made possible by the use of refocusing radiofrequency pulses, as applied in spin-echo pulse sequences. However, while spin-echo sequences are used, the most common approach is to leverage the strong susceptibility-based contrast mechanism, sampled by gradient-echo sequences[26]. The non-refocusing, gradient-echo pulse sequence, is repeated over time and as the contrast agent passes through the tissue of interest, its strong effect on the transversal relaxation produces a temporary decrease in signal that can be observed[30]. Depending on brain coverage and spatial resolution, typical sample rates used in practice are 0.5-1.5 s.

The DSC-MRI sequence used in paper I and II was based on a segmented gradient echo echo-planar imaging (EPI) sequence with 2 segments, producing an image every 1000 ms, with echo time 30 ms, flip angle 40 degrees, repetition time 500 ms. Slice thickness was 5 mm with no slice gap, the in-plane voxel dimensions were 1.8×1.8 mm^2, field of view was 230×230 mm^2 and acquisition matrix 128×128.

Gadolinium-based contrast agent

The tracer used in the DSC-MRI acquisition is a paramagnetic contrast agent, commonly based on a gadolinium-chelate. The chelate acts as a carrier-molecule, designed to encapsulate the toxic metal during its passage through the human body. The tracer is commonly injected via the right antecubital vein, passing through the pulmonary circulation before arriving at the brain, where its effect on the image contrast can be measured. In paper I and II a gadopentetate-based contrast agent (Gd-DTPA 0.5 mmol/ml) was administered at 5 ml/s of 0.1 mmol/kg, followed by a saline flush of 10 ml. In light of the recent debate on gadolinium deposition and the risk of developing nephrogenic systemic fibrosis[31], it should be mentioned that the used contrast agent has since the acquisition of the current dataset been banned for use in the EU.

Estimation of tracer concentration from MR signal

By use of a gradient echo sequence, change in MR signal depends on the change in transversal relaxation rate according to

$$S(t) = S_0 e^{-TE \Delta R_2^*(t)} \tag{1}$$

The change in transversal relaxation rate $\Delta R_2^*(t)$ is approximately linearly related to the contrast agent concentration[29]. This linear approximation enables a simplified observational model for the tissue contrast agent concentration

$$\Delta R_2^*(t) = r_2^* \, C_{tis}(t) \tag{2}$$

The estimation of contrast-agent concentration from MRI signal can then be formulated

$$r_2^* \, C(t) = -\frac{1}{TE} ln\left(\frac{S(t)}{S_0}\right) \tag{3}$$

Model theory

Tracer kinetic modeling, also known as the Meier-Zierler indicator-dilution theory[32], describes a model of the tissue microvasculature and the formulation of equations expressing perfusion parameters that are commonly used in intravascular bolus tracking techniques. The application of this theory is not limited to the brain or even perfusion imaging, but its most common applications include contrast agent-based techniques such as DSC-MRI and DCE-CT. While outside the scope of this thesis, the theory can be expanded to include the case where a permeable vasculature leads to contrast agent extravasation. Such a vasculature is characteristic for the brain with a disrupted BBB or in other organs of the body.
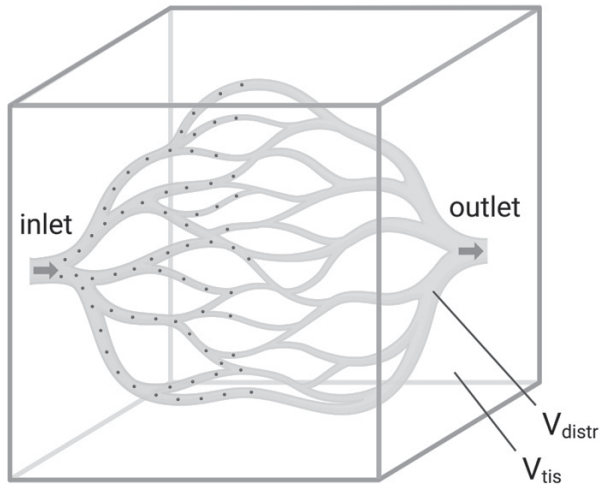
Figure 3. *System representing the microvasculature with a bolus of intra-vascular tracer particles passing through.*

Under the assumption of an intravascular tracer, the tissue is assumed to behave in accordance with a linear and time-invariant system as illustrated in Fig. 3. More specifically, the system is assumed to fulfill the following set of properties[32]:

- There exists only one inlet and one outlet to the system.
- The system consists of several pathways of different length of which tracer particles can pass through.
- Tracer particles that enter the system at the same time will thus exit the system via the outlet at different times, producing a distribution of *transit times*
- The system is linear and time invariant, meaning that the distribution of transit times for particles traversing the system is the same regardless of the *number* of incoming tracer particles or *when* they enter the system.
- The system holds a constant volume, V_{distr}, and the volumetric flow rate, F, through the system is constant. Tracer particles cannot be trapped in the system and recirculation of tracer particles does not occur, implying that eventually all tracer particles will exit the system.
- The flow of the tracer through the system is representative of the flow of the native medium through the system. This implies that the transit time distribution of the tracer equals that of the native medium.

The distribution of tracer times, $h(t)$, represents the probability that a tracer particle that entered the system via the inlet at time t = 0, will exit through the outlet at time t. Since all particles at some point will leave the system,

$$\int_0^\infty h(\tau)d\tau = 1. \tag{4}$$

The cumulative distribution function, H(t), describes the fraction of all tracer particles that entered the system at t=0 and that have reached the outlet before time t.

$$H(t) = \int_0^t h(\tau)d\tau, \tag{5}$$

the remaining fraction of particles in the system will reach the outlet at a time point after time t, as expressed by the impulse residue function[33],

$$R(t) = 1 - H(t) = 1 - \int_0^t h(\tau)d\tau, \tag{6}$$

The following paragraph will show the relationship between R(t), the measured tissue concentration and concentration at the input to the system. Here, the use of the whole tissue concentration is practical as this is what can be measured remotely in an imaging voxel. Conveniently, with an intravascular tracer, the number of tracer particles in the system, $Q_{V_{distr}}$, equals the number of tracer particles in the whole tissue volume, $Q_{V_{distr}} = Q_{V_{tis}}$. At a given time, t, the number of particles in the system is equal to the difference in the total number of particles that have entered and left the system so

$$Q_{V_{distr}}(t) = Q_{V_{tis}}(t) = Q_{in}(t) - Q_{out}(t). \tag{7}$$

The total number of particles that have passed the inlet and can be expressed as

$$Q_{in}(t) = F \int_0^t C_{in}(\tau)d\tau \tag{8}$$

The general approach to experimental applications of linear systems theory is to sample the system at its inlet and outlet. However, it is possible and in some remote sensing scenarios helpful to instead describe the concentration at the

outlet, by use of the cumulative distribution function, $H(t)$. The total number of particles that have passed the outlet, $Q_{out}(t)$, can then be expressed as

$$Q_{out}(t) = F \int_0^t C_{out}(\tau)d\tau$$

$$= F \int_0^t C_{in}(\tau)H(t-\tau)d\tau \qquad (9)$$

Expressing Eq. 7 with concentrations at the inlet and outlet using Eq. 8 and 9 yields[33]

$$Q_{V_{tis}}(t) = F \int_0^t C_{in}(\tau) - C_{out}(\tau)d\tau$$

$$= F \int_0^t C_{in}(\tau)\big(1 - H(t-\tau)\big)d\tau \qquad (10)$$

Using Eq. 6 this can be written using the residue function[34], as

$$Q_{V_{tis}}(t) = F \int_0^t C_{in}(\tau)R(t-\tau)d\tau, \qquad (11)$$

The division of $Q_{V_{tis}}(t)$ by V_{tis} provides an expression for $C_{V_{tis}}(t)$ as

$$C_{V_{tis}}(t) = \frac{F}{V_{tis}} \int_0^t C_{in}(\tau)R(t-\tau)d\tau$$

$$= \frac{F}{V_{tis}} C_{in}(t) \otimes R(t), \qquad (12)$$

where $\otimes$ denotes the convolution integral and where the assumption of equal contrast-agent relaxivity (Eq. 3) in the feeding artery and the tissue of interest, r_2^*, can be divided out. Eq. 12 shows the relationship between the tissue concentration time curve, the concentration time curve measured at the system inlet, and the tissue impulse residue function.

AIF and experimental considerations

In the experimental setting, $C_{in}(t)$ is referred to as the arterial input function (AIF) and an often-used nomenclature for the AIF is $C_a(t)$, which will be used for the continued derivation of perfusion estimates.

A common site to manually register the global AIF is the middle cerebral artery, but AIF selection can also be aided by the use of an algorithm designed to select the most suitable AIF candidate voxels, based on a number of curve criteria such as early bolus arrival, steep up- and down-slope, avoiding curves with distorted peaks[35,36].

Hematocrit

The contrast agent resides in the blood plasma space while the aim is to quantify perfusion properties of whole blood. Since hematocrit differs between macro- and microvasculature[37], quantification of perfusion requires a correction for hematocrit. Correction factors can be obtained by dividing the tissue concentration time curve and the AIF by the fractional plasma space (1-Hct), in Eq. 13, correction for arterial-, Hct_{art}, and capillary hematocrit, Hct_{cap}, have been combined to one factor as,

$$K_H = \frac{(1-Hct_{art})}{(1-Hct_{cap})},$$ (13)

which when applied to Eq. 12, provides

$$K_H C_{V_{tis}}(t) = \frac{F}{V_{tis}} C_a(t) \otimes R(t)$$ (14)

Estimates of CBF, CBV and MTT

In the following sections, the remaining derivation of perfusion parameters includes experimental aspects such as hematocrit and the estimated residue function, $\widehat{R}(t)$. Maps of parameters CBF, CBV and MTT are shown in Fig. 4.

CBF

The estimation of the residue function from Eq. 14 involves deconvolving the AIF from the tissue concentration-time curve. The inverse problem can be formulated to yield the scaled impulse residue function as[24]

$$\widehat{R}_F(t) = C_a(t) \otimes^{-1} K_H C_{V_{tis}}(t), \tag{15}$$

Where the correction for hematocrit can be applied to $C_{V_{tis}}(t)$ prior to deconvolution, and where the flow scaled impulse residue function $\widehat{R}_F(t) = \frac{F}{V_{tis}} \widehat{R}(t)$. Here, $\widehat{R}(t)$ is an estimate of $R(t)$, representing the fraction of tracer that remains in the system upon an instantaneous deposition of contrast agent at time t=0, thus $R(0) = 1$. However, the numerical solution to Eq. 15 may not be monotonically decreasing, so in practice, the approximation $\max[\widehat{R}_F(t)]$, is used rather than $\widehat{R}_F(0)$.

$$CBF = \max[\widehat{R}_F(t)] \tag{16}$$

CBV

To arrive at the CBV, a short detour to the model in Fig. 3 is necessary. In the case of an intravascular tracer, the number of particles of the whole tissue is the same as the number of particles in the tracer distribution volume.

$$Q_{V_{tis}}(t) = C_{V_{tis}}(t) \cdot V_{tis} = C_{V_{distr}}(t) \cdot V_{distr} \tag{17}$$

Based on the conservation of mass, the total numbers of particles having passed the systems inlet, outlet and distribution space must be equal[34,38].

$$Q_{tot} = F\int_0^\infty C_{in} dt = F\int_0^\infty C_{out} dt = F\int_0^\infty C_{V_{distr}} dt \tag{18}$$

If Eq. 17 is valid for any timepoint, it is also valid for integrations, which enables the substitution of $\int_0^\infty C_{V_{distr}}(t)dt$ from Eq. 18 and the blood volume fraction, can be expressed[34]

$$\frac{V_{distr}}{V_{tis}} = \frac{\int_0^\infty C_{V_{tis}}(t)dt}{\int_0^\infty C_{V_{distr}}(t)\,dt} = \frac{\int_0^\infty C_{V_{tis}}(t)dt}{\int_0^\infty C_{in}(t)\,dt}. \tag{19}$$

In neuroimaging scenarios, the volume fraction is known as the CBV. Here, the correction for hematocrit has also been added.

$$CBV = K_H \frac{V_{distr}}{V_{tis}} = K_H \frac{\int_0^\infty C_{V_{tis}}(t)\,dt}{\int_0^\infty C_a(t)\,dt} \tag{20}$$

This derivation enables CBV estimates without deconvolution. The measures provide volume-specific estimates (in relation to 100 ml tissue), but mass-specific estimates of CBF and CBV are given via division by the tissue density.

MTT
It can be shown that MTT is related to R(t) as follows[24,25,32]

$$MTT = \int_0^\infty t\, h(t)dt = \int_0^\infty R(t)dt \tag{21}$$

In practice, this is achieved after deconvolution as

$$MTT = \frac{\int_0^\infty \widehat{R}_F(t)dt}{\max[\widehat{R}_F(t)]}, \tag{22}$$

which has been referred to as the Zierler's area-to-height relationship.

Central-volume theorem and alternative forms
Finally, the central-volume theorem[32,39] states that the relationship between these parameters is $CBV = CBF \cdot MTT$. This relationship between the three perfusion parameters enables alternative formulations by its use together with two of the three above expressions for CBF, CBV and MTT[25].
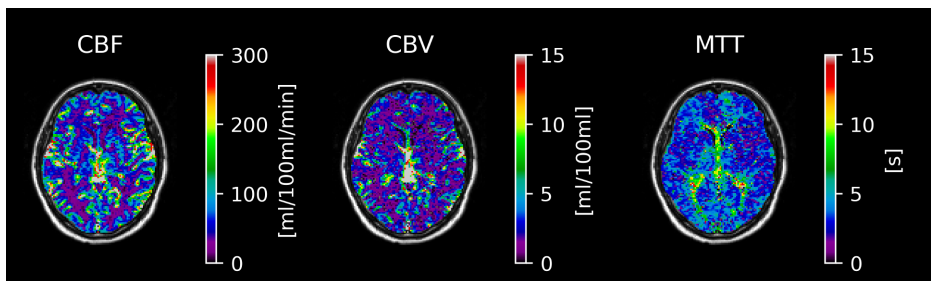

Figure 4. Parameter maps of CBF (left), CBV (center) and MTT (right) resulting from a standard DSC-MRI acquisition of a healthy elderly subject, overlayed on a fluid attenuated inversion recovery image. CBF and CBV have been scaled such that CBV in white matter is 2 ml/100ml.

Deconvolution

Signal representation-based analyses have been suggested also within the field of DSC-MRI[40–42], but the most common approach is to solve the inverse problem in Eq. 15, as illustrated by Fig. 5. In other words, to deconvolve the AIF from the tissue concentration-time curve.

At noise levels typical for experimental scenarios, the inverse problem of Eq. 15 is ill-posed, meaning that there exist many solutions to it. This inverse problem is also regarded ill-conditioned, meaning that small variations in the measured data can have large effects on the solution. Over the last two and a half decades, this has led to the development of many deconvolution strategies[43–57].
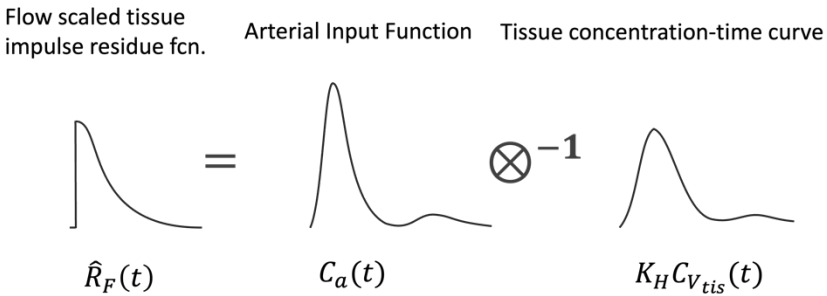

Flow scaled tissue impulse residue fcn.   Arterial Input Function   Tissue concentration-time curve

$$\hat{R}_F(t) \qquad\qquad C_a(t) \qquad\qquad K_H C_{V_{tis}}(t)$$

Figure 5. *Illustration of inverse problem with the flow scaled tissue impulse residue function, the AIF and the tissue concentration-time curve.*

Eq. 14 can be written on discrete form as

$$K_H C_{V_{tis}}[t_j] = dt\, CBF \sum_{i=0}^{j} C_a[t_i] \cdot R[t_j - t_i], \qquad (23)$$

where dt is the sampling interval and where the convolution instead can be reformulated using matrix notation,

$$c_{V_{tis}} = \boldsymbol{A} r \qquad (24)$$

in which, $\boldsymbol{A}$, approximates the AIF-convolution integral and where K_H, dt, and CBF constants have been included in $c_{V_{tis}}$, $\boldsymbol{A}$ and r, respectively.

If the inverse of $\boldsymbol{A}$ could be derived, the solution would be trivial:

$$\boldsymbol{A}^{-1}c_{V_{tis}} = r. \tag{25}$$

The convolution theorem enables the use of the Fourier transform, often regularized by low pass filtering to stabilize the solution in the presence of noise [46]. But these techniques have proven sensitive to noise[58].

SVD

Singular value decomposition (SVD)[43,44] can be used to achieve the so-called More-Penrose pseudoinverse of $\boldsymbol{A}$, $\boldsymbol{A}^+$. By decomposing the convolution matrix into left and right singular matrices $\boldsymbol{U}$ and $\boldsymbol{V}^*$, which are made up of the eigenvectors of $\boldsymbol{A}\,\boldsymbol{A}^T$ and $\boldsymbol{A}^T\boldsymbol{A}$, respectively.

$$\boldsymbol{A} = \boldsymbol{U}\boldsymbol{\Sigma}\boldsymbol{V}^*$$

The covariance matrix, $\boldsymbol{\Sigma}$, of such a decomposition is diagonal and thus invertible, and made up of the square root of the eigenvalues of $\boldsymbol{A}\,\boldsymbol{A}^T$ or $\boldsymbol{A}^T\boldsymbol{A}$, the so-called singular values. The singular values of $\boldsymbol{\Sigma}$ are all positive and normalized to the largest singular value and placed in a descending order such that the first value equals 1. SVD can be used to find the pseudoinverse, $\boldsymbol{A}^+ = \boldsymbol{U}^*\boldsymbol{\Sigma}^{-1}\boldsymbol{V}$, which in turn can be applied in Eq. 25 as

$$\boldsymbol{U}^*\boldsymbol{\Sigma}^{-1}\boldsymbol{V}c_{V_{tis}} = r. \tag{26}$$

However, as with Fourier-based deconvolution, solutions are often afflicted by non-physiological oscillations. Such oscillations can be addressed by applying a threshold to the values of $\boldsymbol{\Sigma}^{-1}$ to provide a smoother solution, effectively allowing fewer components of the AIF to form c_{tis}. The standard SVD (sSVD) based technique has been subject to improvements such as the delay-insensitive block-circulant design of the $\boldsymbol{A}$-matrix (cSVD) and the oscillatory index-based selection of singular value threshold, as a means to yield solutions with similar degrees of oscillations (oSVD)[44]. The use of oSVD has been wide-spread and has seen use as a method of reference in the development of novel deconvolution strategies[47,48,52,59]. In this thesis, oSVD was used in the evaluation of injection duration effects in paper I.

Numerical solutions

A numerical approach to solving Eq. 24 is to find the vector, r, which minimizes

$$r = \min_{r}\{\|Ar - c_{V_{tis}}\|\}. \tag{27}$$

A penalty term can also be added to steer the optimization toward a solution that agrees with expectations on a physiologically plausible solution.

$$r_{\lambda} = \min_{r}\{\|Ar - c_{V_{tis}}\| + \lambda\|Lr\|\}, \tag{28}$$

where λ is the regularization parameter and where the matrix $\boldsymbol{L}$ is designed to introduce a penalty when the solution, r, deviates from *a-priori* expectations on the solution. Typically, such expectations address the smoothness of the solution[45], but also monotonicity can be addressed.

Vascular model

Vascular model-based analyses were proposed in early studies by Kroll et al.[60] and Østergaard et al.[61]. Mouridsen et al.[47] continued on this path by assuming that the distribution of transit times, *h(t)*, follows a gamma variate distribution.

$$h(t; \alpha, \beta) = \frac{1}{\beta^{\alpha}\Gamma(\alpha)} t^{\alpha-1} e^{-t/\beta} \qquad \alpha, \beta > 0 \tag{29}$$

Where α and β are shape parameters. By inserting $h(t; \alpha, \beta)$ in Eq. 6, the impulse residue function is

$$R_{vm}(t; \alpha, \beta) = 1 - \int_{0}^{t} h(\tau; \alpha, \beta) d\tau \tag{30}$$

The implementation of vascular model deconvolution includes an additional parameter, δ, to account for delay between the AIF and the tissue concentration time curve.

$$C_{vm}[t_j; \Theta] = dt\, CBF \sum_{i=0}^{j} C_a[t_i - \delta] \cdot R_{vm}[t_j - t_i; \alpha, \beta] \tag{31}$$

Where Θ are the model parameters $(\alpha, \beta, \delta, CBF)$.

In practice, the convolution in Eq. 31 is performed on up-sampled curves and using a Volterra convolution matrix[62] to minimize errors related to the discrete approximation of the convolution integral. Finally, the model can be fitted in the signal domain by applying the observational model, Eq. 1, and the linearity assumption in Eq. 2 as

$$S[t; \Theta] = S_0 e^{-TE r_2^* C_{vm}[t; \Theta]} + \varepsilon, \tag{32}$$

where, ε represents a gaussian noise vector. Note, that the inclusion of the hematocrit correction factor, K_H, was left out of this paragraph for sake of simplicity. In paper II, vascular model-based deconvolution was implemented in a Bayesian fitting scheme as described by Mouridsen et al.[63] and used for the estimation of relative perfusion.

Nonparametric deconvolution

A closely related strategy to the vascular model is to use Eq. 31 but implement an alternative description of the flow scaled residue function. Many approaches exist[48–53,55]. These techniques typically require the fitting of a number of parameters, and many utilize Bayesian model fitting schemes. While these methods do not assume a specific shape of the solution, regularization and intrinsic properties of the methods may result in shape restrictions on the solution.

Challenges of absolute quantification

DSC-MRI is faced with a number of challenges that stand in the way of absolute quantification of perfusion parameters. A number of reviews on this topic that are well worth reading have been published, including Knutsson et al. 2010[26], Willats et al. 2013[64] and Calamante 2013[65]. Several of these challenges are associated with the fact that a global AIF is commonly used as a surrogate measure for the concentration-time curve at the inlet of the system. Delay and dispersion (temporal widening) of the bolus of contrast occurring between the site of registration and the tissue of interest will then risk obstructing the perfusion estimation. While corrections for delay are possible to incorporate in deconvolution methods and appear to work relatively well, the effect of AIF-dispersion is more challenging. In patients with vascular abnormalities, dispersion has been shown to have substantial impact on perfusion estimates[66,67], sparking research on use of local AIFs[68–72]. The use of a global AIF, however, remains the most common approach, with dispersion correction as an optional addition to the inverse problem of perfusion estimation[49,52,55,73].

Partial volume effects and misregistration of the AIF are also of major importance. Kjölby et al.[74] showed via simulations how partial volume and the orientation of the vessel relative to the static magnetic field, B_0, affects the shape of the AIF. Furthermore, the alternative of selecting an AIF-voxel entirely within the artery is less viable, mainly due to the limited spatial resolution and the signal saturation that such a voxel would cause, given that the imaging is optimized towards a strong signal response from tissue. The best alternative to obtain a non-distorted and minimally broadened AIF appears to be in a voxel with small partial volume of an artery that is oriented in parallel to B_0. While this approach may produce an AIF with preserved curve shape properties, the partial volume effect will still directly scale estimates of CBV and CBF and needs to be addressed[74]. Several approaches have been proposed to address AIF partial volume effects, including a novel sequence that simultaneously excites a slice in the neck region with short echo time and complex signal read out[75], or the addition of phase data as a basis for partial volume correction[76]. Also, methods based on rescaling the AIF have been proposed, such as the rescaling based on the ratio of the area under the tails of the measured AIF and venous output function[77], as well as a scaling scheme based on an additional small dose pre-bolus contrast agent administration[78].

Further challenges that can be considered include macrovascular partial volume contributions to the measured tissue signal, leading to errors in parameter estimates[59,64]. Such correction has been addressed by modeling macrovascular within-voxel contributions to concentration as a relative arterial blood volume-scaled AIF[59]. Contrast agent extravasation, leakage from the vasculature to the extravascular, extracellular space can be addressed by adopting a leakage term from dynamic contrast enhanced MRI (DCE-MRI) models[79]. Leakage in clinical rCBV-estimates is commonly addressed by so called Boxerman-Schmainda-Weisscoff-correction, based on a linear fitting algorithm[80].

The effects of injection speed, which translates to injection duration given a volume of tracer, has been studied in silico by van Osch et al.[81] The injection of a volume of tracer ultimately determines the time duration of the input function with which to observe the tissue response. In paper I, we build upon these results, to evaluate the effect of injection duration on quantitative perfusion estimation under experimentally relevant noise conditions of DSC-MRI and DCE-CT perfusion.

Simulation of bolus tracking data

The simulations in paper I were performed to enable the evaluation of perfusion estimation with predefined perfusion parameters, injection durations and noise levels. A detailed description for both DCE-CT and DSC-MRI curves are included in paper I, here a short description of DSC-MRI curves is included and illustrated in Fig. 6.

Tissue concentration-time curves were derived by use of the vascular model in Eq. 31, with shape parameters of the impulse residue function fixed $\alpha_{res} = 3$ and where $\beta_{res} = MTT/\alpha_{res}$. The AIF was modelled as a box-car function representing the injection of contrast agent convoluted with a gamma-variate dispersion kernel, $\varphi(t; \alpha, \beta)$, (same as in Eq. 29) with $\alpha_{disp} = 3$ and $\beta_{disp} = 1.8$, representing the pulmonary circulation. Recirculation was modelled as a delayed, dampened, and dispersed copy of the first pass, providing the AIF as

$$C_a(t) = \left(B(t) + e^{-\lambda\delta}B(t - \delta) \otimes \varphi(t; \alpha, \beta)\right) \otimes \varphi(t; \alpha, \beta), \qquad (35)$$

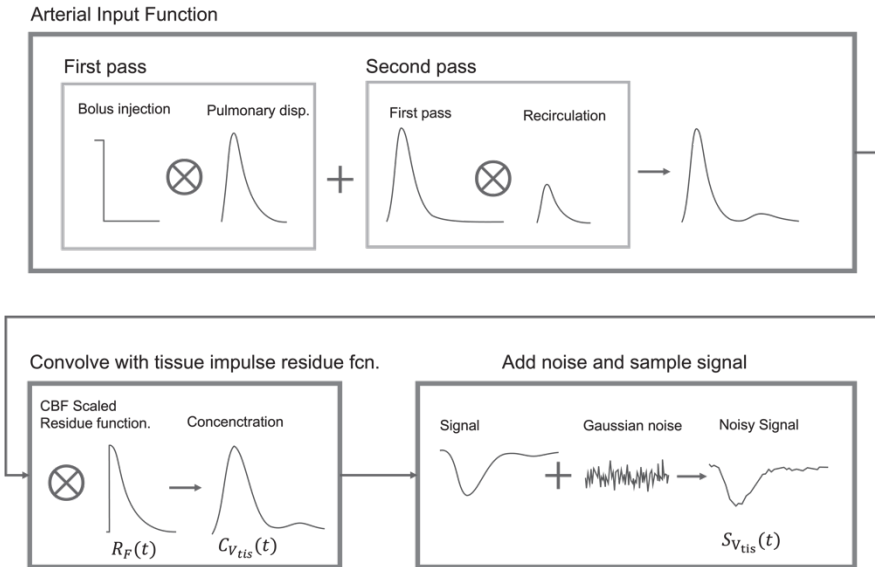Where the recirculation parameters were set to $\lambda = 0.13$ s^{-1} and $\delta = 16$ s.

Figure 6. *Schematic diagram of the simulation of a noisy tissue signal-time curve.*

Concentration time curves were transformed to the signal domain using the observational model and linear assumption in Eq. 1 and 2, as

$$S(t) = S_0 e^{-K \cdot TE \cdot C(t)} \tag{36}$$

Where S_0=100 and K, which accounts for both hematocrit and the linearly assumed tissue relaxivity, was set to achieve a 40% signal drop at maximum concentration in a reference tissue with CBF = 60 ml/100ml/min. For the AIF, a 60 % maximum signal at peak concentration was set.

Gaussian noise was finally added in the signal domain, where the contrast-to-noise (CNR) was defined in the concentration domain such that

$$CNR = \frac{C_{max}}{\sigma_{baseline}}, \tag{37}$$

Where C_{max} is the maximum concentration and $\sigma_{baseline}$ is the standard deviation of the baseline concentration[81].

PERIPHERAL MUSCLE BOLD PERFUSION

The interest in peripheral muscle function has grown, partly due to global aging and the concomitant rise in musculoskeletal disorders[82]. The application of functional MRI techniques has also provided new possibilities for probing peripheral muscle tissue perfusion and metabolism. For that purpose, a number of candidate MR techniques are under development, and amongst these, ASL, BOLD, ASL, intravoxel incoherent motion (IVIM) and DCE-MRI, ^{31}P magnetic resonance spectroscopy (MRS) and chemical exchange saturation transfer (CEST) have been considered promising[82,83].

DCE-MRI has been applied to peripheral muscle perfusion and showed differences in time curves between muscles. DCE-MRI has the potential to provide the widest array of perfusion parameters out of these. So far estimates of the hyperemic microvascular blood plasma volume fraction of the musculature have been presented as an interesting potential biomarker for PAD assessment[84]. ASL and IVIM can both provide quantitative measures of blood flow and neither technique requires an intravenous contrast agent injection. In a recent study, both ASL-blood flow and IVIM-f and -D* showed significant differences between pre- and post-operative measures in several calf muscles of which those in the anterior and soleus muscles correlated with pre- and post-operative ABI improvement[85]. Phosphocreatine (PCr) measured by ^{31}P-MRS is a surrogate for mitochondrial function and prolonged recovery after exercise is a marker of skeletal muscle ischemia in PAD[86]. Unfortunately, the technique requires long acquisition times and lacks spatial resolution[83]. An alternative to ^{31}P-MRS is to perform creatine chemical exchange saturation transfer crCEST, in which relatively high-resolution images reflecting creatine levels can be acquired repeatedly after exercise, to monitor recovery. crCEST is a promising technique, but further studies were found necessary to validate the technique[87].

Paper III and IV, focuses on leveraging the BOLD contrast, which is sensitive to the ratio of oxygenated-Hb/deoxygenated-Hb in the tissue. The technique does not require any external contrast agents, and the relatively low noise level and high temporal resolution of repeated acquisitions over time are beneficial properties. An important aspect of peripheral muscle BOLD imaging is how contrast changes can be introduced by imposing blood flow restrictions to feeding arteries as first described by Toussaint et al.[88]. This enables the possibility to gain insights from the tissue of interest at both ischemic and hyperemic states.

BOLD contrast mechanism

The blood oxygenation level-dependent (BOLD) effect in MRI is highly complex with many simultaneous effects[89]. Simplified, however, it can be summarized as a change in T_2 and T_2^* due to the change in the ratio of deoxygenated and oxygenated hemoglobin (Hb) in the tissue. The shortening effect is caused by the paramagnetic property of deoxygenated Hb inducing microscopic magnetic field inhomogeneities in the blood and tissue surrounding the capillaries, in turn, leading to increases in bulk susceptibility[89].

Since the research field of peripheral muscle BOLD imaging is relatively new, theory is lacking in regard to muscle specific BOLD mechanism, and especially in combination with cuffing techniques that induce ischemia and subsequent hyperemia. The research field of functional MRI (fMRI), on the other hand, has applied BOLD contrast to dynamically image the brain since its discovery in the early 1990s[90]. Within the fMRI research, substantial efforts have been made toward establishing biophysical models that can accurately capture the BOLD contrast mechanisms involved in neuronal activation[91]. Two main modeling strategies have been established, 1) Dynamic physiological modeling and 2) steady state calibration methods. Dynamic biophysical models are utilized in the analysis of data acquired with task-based paradigms and aim to quantify the dynamic physiological response to a stimulus. Calibration methods aim to produce estimates of oxygen metabolic parameters such as oxygen extraction fraction (OEF) and cerebral metabolic rate of oxygen ($CMRO_2$). Such methods often utilize hypercapnic (elevated CO_2) or hyperemic (elevated O_2) respiratory paradigms and an imaging sequence that enables simultaneous BOLD and ASL acquisitions, to provide estimates of CBF for use in the analysis.

Within the research of calibration methods, Griffeth and Buxton presented a detailed four-compartment BOLD signal model that is valid under ideal noise-free conditions[92], as

$$\frac{\Delta S}{S_0} = H\big(V_E e^{-TE \cdot \Delta R_{2E}^*} + \varepsilon_A V_A e^{-TE \cdot \Delta R_{2A}^*} + \varepsilon_C V_C e^{-TE \cdot \Delta R_{2C}^*} + \\ \varepsilon_V V_V e^{-TE \cdot \Delta R_{2V}^*}\big), \tag{38}$$

where

$$H = 1/\big(V_E + \varepsilon_A V_{A,0} + \varepsilon_C V_{C,0} + \varepsilon_V V_{V,0}\big). \tag{39}$$

Table 2 provides symbol keys and Fig. 7 illustrates the four compartments considered.

Table 2. *Symbol keys for BOLD signal model.*

| Symbol	Symbol keys
S	BOLD signal
S_0	Baseline BOLD signal
ΔS	$S - S_0$
$V_{(E,A,C,V)}$	Volume fractions (intravascular, arterial, capillary, venous)
$V_{(E,A,C,V),0}$	Baseline volume fractions (intravascular, arterial, capillary, venous)
$\varepsilon_{(A,C,V)}$	Signal ratio at baseline of an intravascular volume (arterial, capillary, venous) to an extravascular volume
$\Delta R_{2(E,A,C,V)}^*$	Change in MR signal relaxation rate with stimulus for each compartment (extravascular, arterial, capillary, venous)
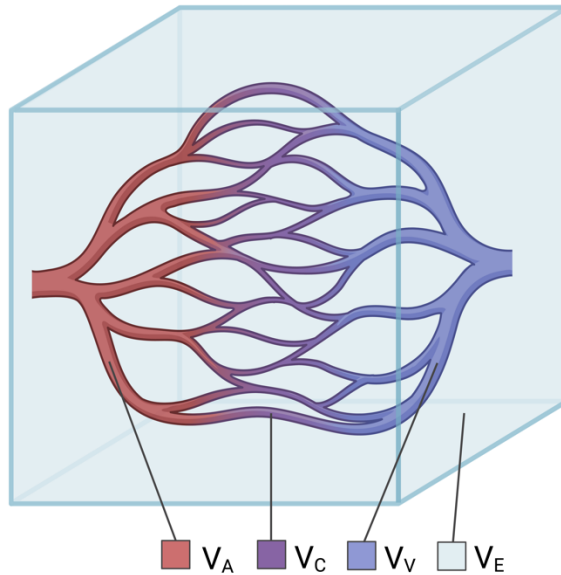
Figure 7. *Illustration of vascular (arterial, capillary, venous) and extravascular compartments that contribute to the BOLD effect.*

According to this four-compartment BOLD model, the T_2^*-relaxation in gradient-echo BOLD imaging is influenced by the extravascular volume, and three intravascular volume compartments. The intra- and extravascular compartments can be considered separately since exchange rates are slow in relation to the imaging echo time (TE)[92]. This model describes the effect on the BOLD contrast at an impulse in relation to baseline. Note that, in addition to the variation in the relaxation rates, the volume fractions of each compartment, $V_{(E,A,C,V)}$ and $V_{(E,A,C,V),0}$, can differ between the two measurements, providing an increasing degree of complexity due to such physiological change[93].

A detailed review of physiological and biophysical BOLD-effects was made by Kim and Ogawa (2012)[89] showing that not only the blood oxygen level dictates the measured signal. Water molecule diffusion contributes to deoxygenated-hemoglobine-induced signal dephasing in the extravascular compartment. This effect is strong for capillaries, but not for larger vessels[94]. Additionally, T_2^*-relaxations will depend on vessel diameters and the orientation of vessels relative to the static magnetic field B_0. Each compartment will thus depend on this effect to a varying degree. Also, intracellular pH will influence the BOLD signal of the extravascular compartment[95]. The dependency between the BOLD signal, tissue blood flow

and venous blood volume[94], previously studied in dynamic physiological modelling in fMRI, will be valid also for the case of peripheral muscle BOLD imaging. More specifically, increases in the venous oxygenation level caused by an increase in CBF will lead to an increase in the BOLD signal, while increases in the venous blood volume (at the expense of decreases in the volume of other compartments), will lead to a decrease in the BOLD signal resulting from the comparatively higher ΔR_{2V}^* of this compartment[96].

The cuffing paradigm and practical considerations

In practice, cuffing-based peripheral BOLD imaging can be performed by using a tourniquet system and a multi-echo MR sequence, where the cuffing introduces dynamical changes in the tissue oxygenation and the sequence allows imaging of these changes. By the inflation and deflation of the cuff, blood flow restrictions to the muscle tissue of interest and reperfusion can be achieved. In paper III and IV, cuff inflation and deflation were made according to a predefined cuffing paradigm. Such a study design allowed different aspects of calf-muscle ischemia, the hyperemic response, and the transition between these states to be studied. Fig. 8D. shows an example of a measured time curve including the three phases of the cuffing technique, and how a descriptive model is fitted to these data points and subsequently used to derive perfusion related measures.

Scanning procedure

The scanning procedure in peripheral muscle BOLD perfusion requires a correct placement of the leg near the centre of the MR-bore, as well as correct positioning of the thigh tourniquet and MRI coil. Finally, the padding of the leg will ensure stability during the applied cuff-compression scheme and should be optimized also for patient comfort as this decreases the risk of patient movement during scanning. Fig. 8A shows the positioning of the pressure cuff, the MRI flex-coil, and an example of applied padding.

The data acquisition includes dynamic imaging of the peripheral limb during a cuffing scheme consisting of three segments. The first segment is the baseline period when the cuff remains deflated. The baseline is followed by the ischemic segment, where the cuff is inflated. The final segment includes the release of pressure in the cuff, enabling tissue re-oxygenation, the cuff is then kept deflated for the remaining duration of the acquisition. The effect of this cuffing paradigm on calf skeletal muscle can be seen on the BOLD T_2^*-time curve tissue shown in Fig. 8D.
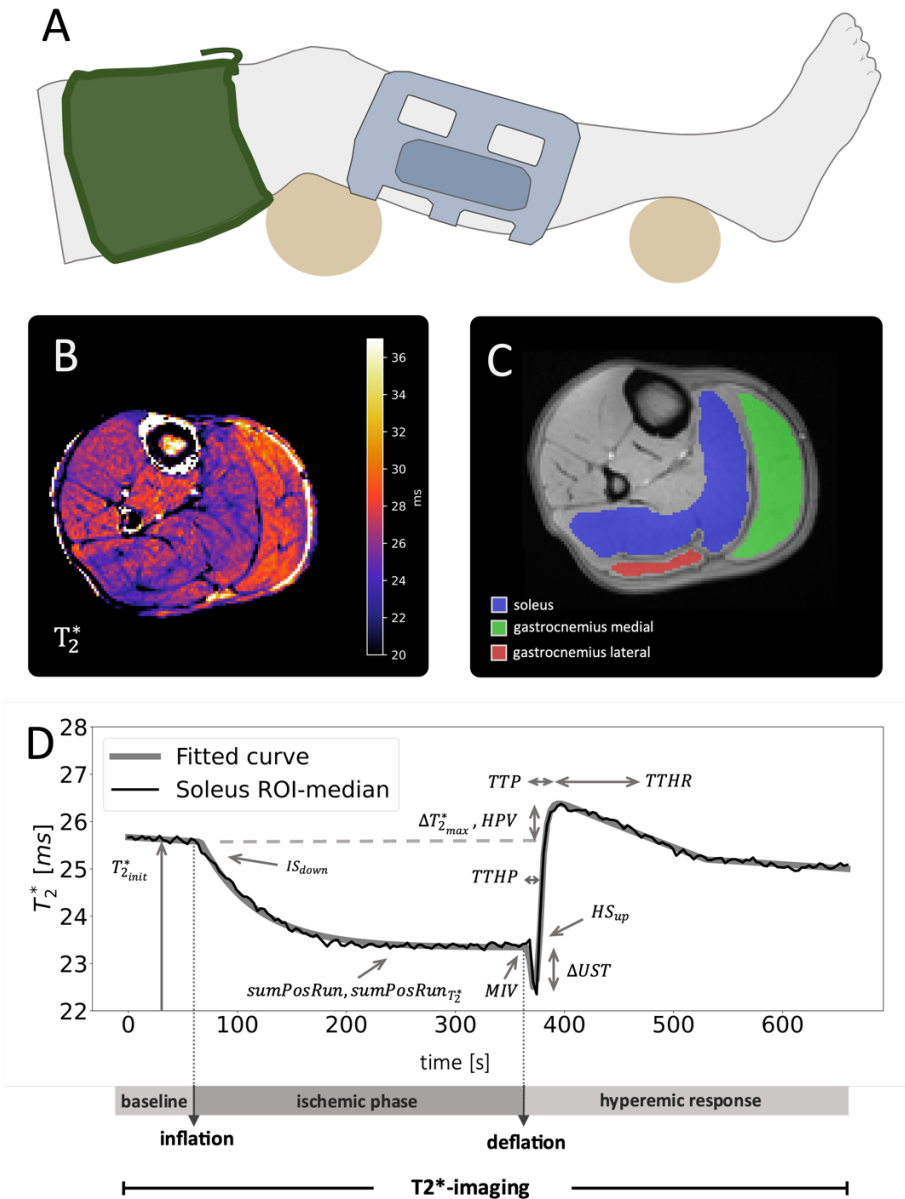
Figure 8. Illustration of experimental setup of peripheral muscle BOLD MR including the positioning of leg with pressure-cuff, coil and padding (A, illustration is inspired by an original artwork by Erika Berggren), T_2^*-map estimated from the first acquisition (B), ROIs delineated in the first-echo, first-acquisition image (C), and an acquired time curve with derived perfusion related measures, as well as the cuffing sequence with the cuff inflation and deflation indicated (B).

Peripheral muscle BOLD MRI

In the literature, BOLD imaging techniques have been applied to skeletal muscle of patients with various cardiovascular diseases. The technique has proven to be able to differentiate between patients with PAD[97–101], critical limb ischemia[102], Type 2 diabetes[103] and systemic sclerosis[104] and controls. Improvements in symptom severity following from surgical revascularizing interventions in PAD[102,105] and treatments in type 2 diabetes patients[106] have also shown to be reflected by the technique.

The adoption of cuff-based peripheral muscle BOLD imaging has since its first publication in the 1990s by Toussaint et al.[88] been slow, possibly due to scanner hardware limitations and limitations in acquired data. However, the last decade has seen an increasing interest[107–113]. There are currently no reference values for derived measures and when results are compared between studies apparent variations in the hyperemic responses of BOLD-time curves are seen. The cuffing duration varies in many of these studies, and as studied in paper III, this will largely dictate the degree of the ischemic provocation.

Regarding scan sequence considerations, there also appears to be substantial variability in how these dynamic BOLD MRI experiments have been performed. For example, Toussaint et al.[88] acquired a single echo (60ms) at 1.5T, Lederman et al.[97] acquired four echoes (16-84 ms) at 1.5T. Partovi et al.[111] acquired four echoes (9.3-41.5 ms) at 3T. Stacy et al.[110] acquired a single echo (40 ms) at 3T and in paper III and IV eleven echoes (2-40 ms) were acquired at 3T, firstly to produce parameter maps as in Fig. 8B, finally via region of interest (ROI) wise analysis (example-ROIs seen in Fig. 8C) to produce T_2^*-time curves and derived perfusion related measures Fig. 8D. In the few mentioned examples above, studies that used more than one echo all displayed curves as baseline normalized T_2^*-time curves. But even so, there are difficulties in comparing the quality of time curves between these studies, as several of them only presents groupwise averaged curves. Interestingly, the original study by Toussaint et al.[88], published almost three decades ago displays a curve with high resemblance to those seen in healthy individuals of paper III and IV (Fig. 8B). The undershooting transient upon cuff-release was observed in this study, but no explanation was given, and the curve trait appears to have received less attention in subsequent studies, until recently (paper IV). The dependency of the quality of acquired T_2^*-time curves on the MRI acquisition appears to be a topic for future standardization efforts.

An interesting approach has been applied by Englund et al. 2013[114], in which an MRI-sequence termed "perfusion, Intravascular Venous Oxygen saturation, and T2*" (PIVOT) is used. The sequence consists of interleaved pulsed arterial spin labeling (PASL) and multi-echo gradient-recalled echo (GRE) sequences. Thus, simultaneously acquiring PASL and multi-echo gradient echo images (5 echoes spanning 3.78-26.32 ms) at 3T. In combination with a cuffing paradigm, this has enabled acquisition of dynamic estimates of T_2^*, oxygen saturation (by use of complex multi-echo gradient echo data) and estimates of blood flow (via PASL data). The possibilities of a combined image acquisition strategy are indeed interesting to consider as a potential tool for monitoring disease progression and effectiveness of treatments, especially if the additional derived parameters can be shown to provide an added diagnostic value. In a second study by Englund et al.[99], TTP estimates from both the dynamic PASL and BOLD acquisitions were found repeatable and sensitive to the presence and severity of PAD. In the MRI acquisitions used in paper III and IV, phase data was acquired for each of the eleven echoes and could be used to derive measures of intravascular venous oxygen saturation as in Englund et al[114]. Even though this was out-of-scope for this thesis, such analysis could potentially add to the ability to separate venous contributions to ROI-wise T_2^*-time curves.

Dynamic BOLD MRI sequence

It has been shown that the use of quantitative T_2^*-mapping provides the benefit of an increased BOLD contrast when compared to T_2^*-weighted imaging[115]. In papers III and IV, multi-echo gradient-echo imaging was used at 3T to acquire 11 equidistant echoes at echo times (TE): 2.0, 5.8, 9.6, 13.4, 17.2, 21.0, 24.8, 28.6, 32.4, 36.2, 40.0 ms. Repetition time was 44 ms and the flip angle was 9 degrees. The single image slice had a thickness of 10 mm, and a field of view of 160×160 mm, with an acquisition matrix of size 128×119. Over the course of the cuffing sequence the MRI-acquisition repeated every 3.2 seconds and for each repetition a T_2^*-parameter map was derived via the fitting of a mono-exponential signal-decay model during data post-processing.

BOLD curve analysis

The four-compartment model, described by Eq. 38 and 39, was designed to describe the signal change between two measurements and includes the volume fractions at both time points, $V_{(E,A,C,V)}$ and $V_{(E,A,C,V),0}$. In the case of a dynamic measurement scenario as in cuff-based peripheral muscle BOLD imaging, this implies estimates for the volume fractions for each time-point of the measurement procedure, $V_{(E,A,C,V)}(t)$. To model such a change, some theory dictating these partial volume changes in response to the cuffing sequence, is required. While Toussaint et al.[88], concluded vasodilation and increased deoxygenated Hb content to be the main contributions to the decrease and increase in signal intensity during ischemia and reperfusion, a more detailed theory of this mechanism is warranted. As this theory is not yet established, the analyses in papers III and IV uses a descriptive, signal representation-based analysis.

The parameterized function (the signal representation) is fitted to a ROI-wise signal- or T_2^*-time-curve to facilitate the quantification of curve shape properties such as levels, slopes, and durations. The design of such a function must be flexible enough to fit to highly variable data, yet specific enough to enable the extraction of meaningful measures, and thus requires a set of underlying assumptions on how a tissue can act in response to the cuffing procedure.

BOLD curve assumptions

The following set of assumptions, also illustrated in Fig. 9, are the bases for the parameterized function. 1) During cuffing, T_2^* will decrease, from a baseline level to an ischemic plateau. 2) Following cuff release, T_2^* will rise steeply to a hyperemic peak. 3) Following the hyperemic peak T_2^* will return slowly to the initial T_2^* level. This minimal set of assumed curve traits can be extended based on observations, to including other shape characteristics. One such example is the post-cuff-release undershoot that was quantified in paper IV.
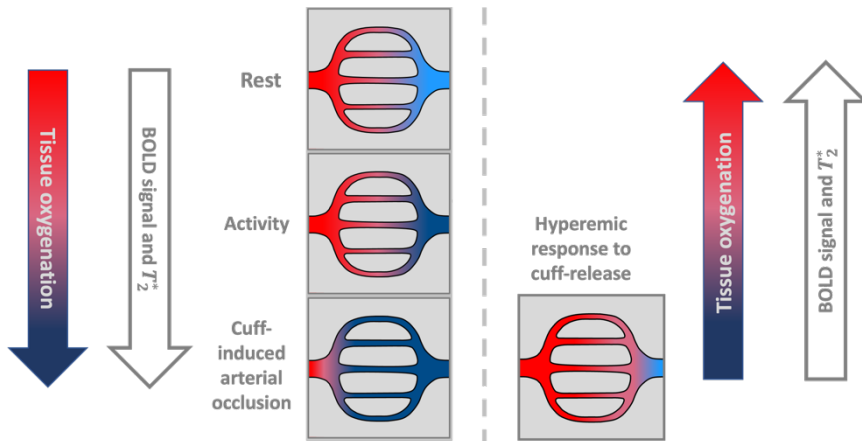
Figure 9. *Assumed BOLD effect in response to activity and arterial occlusion. The color in the illustrated capillary beds represents the degree of tissue oxygenation in the blood. As cuff-induced arterial occlusion takes place, the volume of the venous compartment increases as the available oxygen is consumed. Upon cuff-release, an excess arterial inflow of blood increases the blood oxygenation.*

Signal representation

The signal representation-based analysis in paper III and IV was carried out by the fitting of the function, $f(t, \theta)$, to ROI-wise T2*-time curves. This functional description was developed initially by the company Antaros Medical (Mölndal, Sweden) and has been developed further by the author. Developments include addition of the term u(t), describing the cuff-release undershooting transient as well as various customizations regarding the derivation of the curve measures. The function is comprised by a set of components, defined over specific time intervals as

$$f(t, \theta) = m(t) + n(t) + u(t) + g(t) + s(t) + l(t), \qquad (40)$$

where

$$m(t) = 1 + m_1(t - \frac{t_2}{2}) \qquad\qquad t \leq t_2 \qquad\qquad (41)$$

$$n(t) = m(t_2) - n_0(1 - e^{1 - n_1(t - t_2)}) \qquad t \geq t_2, t \leq t_0 \qquad (42)$$

$$u(t) = n(t_0) + u_0 t(t - t_3) \qquad\qquad t \geq t_0, t \leq t_0 + t_3 \qquad (43)$$

$$g(t) = g_0(1 - e^{-g_1(t - t_0)})e^{-g_2(t - t_0)} \qquad t > t_0 + t_3 \qquad (44)$$

$$s(t) = s_0(1 - e^{-s_1(t - t_0 - t_1)}) \qquad\qquad t > t_0 + t_1 + t_3 \qquad (45)$$

$$l(t) = n(t_0) + l_1(t - t_0) \qquad\qquad t > t_0 + t_3. \qquad (46)$$

Where t_0 is the cuff deflation time point, t_1 is the time from undershoot end until $s(t)$ begins, t_2 is the cuff inflation time point and t_3 is the duration of the cuff-release undershoot. Further, $g(t)$ and $s(t)$, are modifications of the gamma variate and sigmoidal function components, published previously by Schewzow et al.[116], such that the derivative at the upslope of the hyperemic response can be defined. ROI-wise descriptive data representation was carried out by fitting the parameterized function, $f(t, \theta)$, to each T_2^*-time curve.

Perfusion related measures

The measures derived from the described signal representation (Eq. 40) are described in Table 3. Note that since the curve is fitted normalized to baseline, multiplication by the baseline T_2^*-level is necessary to obtain amplitude- and slope-estimates on a ms-scale.

Table 3. *Perfusion related measures and their calculation based on parameters from a signal representation based T_2^*-time curve analysis.*

Measure	Calculation
Baseline T_2^* (ms)	$T_2^*{}_{init} = \dfrac{1}{N_{baseline}} \displaystyle\sum_{j_t \in baseline} \dfrac{1}{N_{ROI}} \sum_{i \in ROI} T_2^*(i, j_t)$
Initial Downslope (ms/s)	$n_0 n_1 T_2^*{}_{init}$
Minimum ischemic value (a.u.)	$(n_{t_0} - m_{t_2})$
Hyperemic Peak Value (a.u.)	f_{max}
Time to half peak (s)	$t^{pre}_{\frac{f_{max}}{2}} - t_0$
Time To Peak (s)	$t_{f_{max}} - t_0$
Hyperemic Upslope (s-1)	$(g_0 g_1 + l_1) T_2^*{}_{init}$
Time to half recovery (s)	$t^{post}_{\frac{f_{max}}{2}} - t_{f_{max}}$
Undershoot transient magnitude (ms)	$-u_1 \left(\dfrac{t_3}{2}\right)^2 T_2^*{}_{init}$

$t^{pre}_{\frac{f_{max}}{2}}$; the time from cuff deflation to reach half-way to the peak T_2^*,

$t^{post}_{\frac{f_{max}}{2}}$; the time from peak T_2^* to reach half-way to baseline level

AIMS

The primary aim of this thesis is to advance the knowledge regarding certain aspects of the acquisition and measurement setup of DSC and BOLD perfusion MRI. The secondary aim is to apply these techniques in clinically relevant patient cohorts, either for the purpose of better understanding the pathophysiology of a disease or for further development of diagnostic imaging procedures. The specific aims of the papers were

I.   to study the effect that the injection duration in DSC-MRI and DCE-CT perfusion has on perfusion parameter estimates

II.   to apply DSC-MRI in an iNPH patient cohort, estimating perfusion pre- and post-operatively in mesencephalon and pons, to explore the involvement of these regions in the pathophysiology

III.   to study the effect that the cuffing duration in cuff-based peripheral muscle BOLD perfusion has on perfusion-related measures in a population of young healthy subjects

IV.   to study and characterize cuff-based peripheral muscle BOLD perfusion T_2^*-time curves and derived measures in PAD patients and healthy controls

SUMMARY OF PAPERS

Paper I

This study evaluates the effect that injection duration and noise have on perfusion parameter estimates in DCE-CT and DSC-MRI perfusion imaging. The simulation-based study design provided ground truth perfusion levels, but also enabled evaluations of these effects both separately and combined. Experimental noise levels typical for ROI-based and voxel-based DCE-CT and DSC-MRI were implemented and perfusion parameters CBF, CBV and MTT were extracted using an oSVD-based deconvolution. A ROI-based analysis based on five healthy subjects scanned using both DSC-MRI and DCE-CT was used to confirm that the simulation-based analysis reflected experimental conditions as shown in the derived estimates from the techniques.

Further evaluations in silico showed that CBF estimates in DCE-CT (with the longer 12.5 s injection-duration) were more prone to a negative bias and increasing variability, compared to DSC-MRI (with the shorter 3.2 s injection duration), especially for high levels of CBF (Fig. 10). CBV was the most robust of the three parameters in regard to injection duration effects and noise.

Increasing noise in tissue time curves to levels typical of single voxel analysis increased the CBF sensitivity to injection duration even further. Hence, the findings strongly suggest that differences in estimates of CBF between DCE-CT and DSC-MRI, to a large degree, can be explained by the different injection durations and noise levels of the techniques.
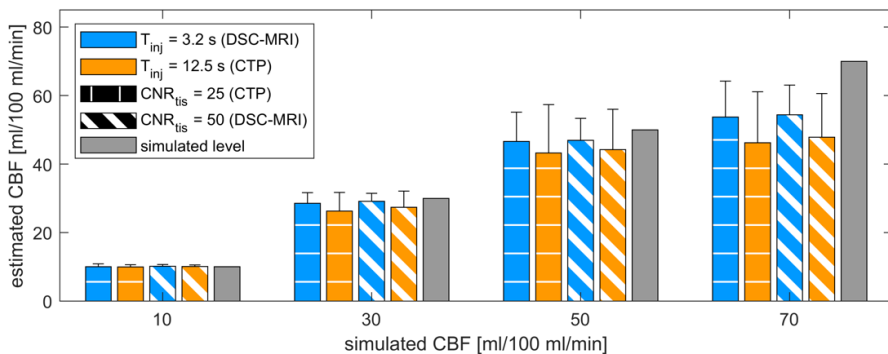

Figure 10. Evaluation of CBF at CBV=4 ml/100ml with noise levels at SNR 50 and 25 and injection durations at 3.2 s and 12.5 s for DSC-MRI and CTP, respectively.

Paper II

Patients with iNPH (n=20) were scanned before and after cerebral shunt surgery using DSC-MRI and diffusion weighted imaging to obtain estimates of relative CBF (rCBF) and apparent diffusion coefficient (ADC). The iNPH-score, a summary score reflecting symptom severity, was acquired pre- and post-operatively and used to distinguish the 15 patients that responded with a ≥5-point improvement to the surgical intervention. An additional age-matched control group (n=15) was subjected to a single session of scanning and iNPH-score measurement.

ADC estimates were obtained from diffusion weighted MRI, scanned with b-values 0 and 1000 s/mm^2 and in 3 orthogonal encoding directions. Perfusion estimates were derived by fitting the vascular model to the AIF and ROI-wise tissue signal-time curves. The fitting procedure was implemented in-house and based on a Bayesian cost function and Maximum Likelihood Expectation Maximization optimization framework. Relative estimates, rCBF, were produced by division with the estimate in the occipital lobe reference-ROI.

iNPH-patients had lower preoperative ADC in the mesencephalon and pons when compared to controls. Postoperatively, ADC decreased but without correlation to clinical improvement. Preoperative rCBF was comparable in preoperative patients and in controls. After surgery, rCBF increased in the responder group in mesencephalon and pons and the increase correlated with clinical improvement as seen in Fig. 11. The alterations in ADC and rCBF in the mesencephalon and pons in iNPH-patients combined with the finding that rCBF increased postoperatively, seem to reflect clinical reversibility in shunt responders and strengthens the hypothesis, that these areas may be involved in the development and potential reversibility of iNPH.
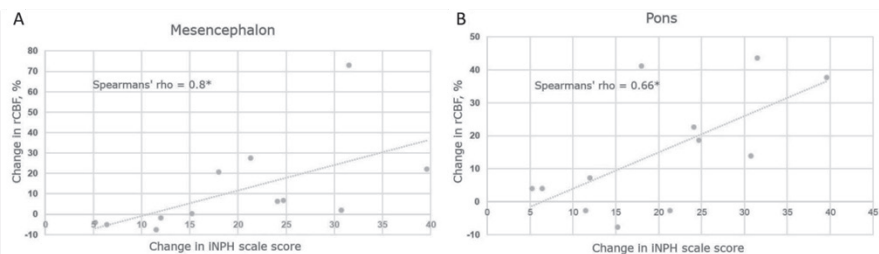

Figure 11. *Correlation between rCBF and post-surgery change in iNPH scale score in responders for mesencephalon (a) and pons (b). This figure is a reprint from Agerskov and Arvidsson et al.* [117]*, available under the CC-BY 4.0 license*

Paper III

The study was set up to evaluate the sensitivity of the cuff-based BOLD imaging technique to the cuffing duration, including changes in BOLD parameters between different durations but also assessment of intra- and inter-scan repeatability. The study was based on a small cohort of young healthy individuals subjected to repeated measurements in which two different cuffing sequences were used, as shown in Table 2.

Table 2. *Data acquisition protocol with the resulting number of included subjects, n, for each imaging session.*

Session	Measurement 1	Rest	Measurement 2
1	5 min occlusion (n=14)	10 min	5 min occlusion (n=10)
2	1.5 min occlusion (n=14)	10 min	1.5 min occlusion (n=11)
3	5 min occlusion (n=6)	-	-

Occlusion, either 1.5 or 5 min, denotes which compression sequence was used for each scan session.

The longer occlusion duration was found to produce an enhanced hyperemic response (Fig. 12A), producing significantly different values in gastrocnemius (as exemplified in Fig. 12B) for all measures describing the hyperemic response, and in soleus for two of these measures. More specifically, the longer 5-minute cuffing yielded an increase in hyperemic-upslope of ~40 % in gastrocnemius and ~60 % in soleus. This was also captured in both muscles by the time-to-half-peak measure which was found shorter by ~50% in gastrocnemius and ~35 % in soleus.
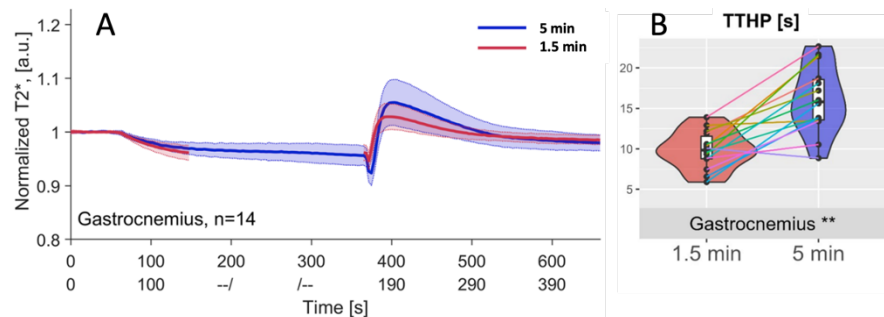

Figure 12. *The groupwise mean (filled) and standard deviation (shaded) of ROI-mean time curves from the gastrocnemius muscle, n=14 (A). TTHP in gastrocnemius for the measurement 1 in session 1 and 2 (B). This figure is based on figures from Arvidsson and Eriksson et al.[113], printed under the CC-BY 4.0 license*

In conclusion, paper III shows that occlusion durations in cuff-based peripheral muscle BOLD imaging indeed influences the dynamics of the hyperemic response in peripheral cuff-based BOLD imaging and that a longer duration enhances the BOLD dynamics

Paper IV

In a structured survey of data from patients with PAD, and age-matched and young controls, deviations from a standard T_2^*-time curve were identified most commonly for PAD patients. For gastrocnemius, curve traits deviating from *the standard curve* (Fig. 13A) included non-monotonic T_2^* decrease during cuffing, 63 % and 33 % (Fig. 13B); transient curve traits linked to cuffing events, 42 % and 67 % (Fig. 13C); and apparent curve dependencies between muscles, 21 % and 0 % (Fig. 13D); for patients and age-matched controls, respectively. The negative cuff-release transient was observed even more frequently in young controls at 92 %. This trait has been included in the parameterized signal representation used in the analysis. The trait has similarities to the pre-impulse undershoot found in fMRI studies and may be relevant to study further from a biophysical and clinical perspective.
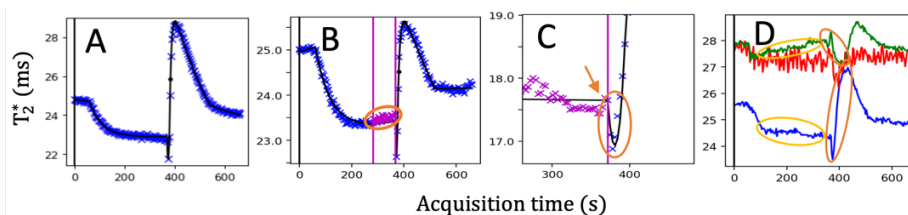
Figure 13. *Examples of soleus T_2^*-time curves (blue and magenta) with orange annotations: the standard curve (A) followed by deviating curve traits including non-monotonic decrease in T_2^* during cuffing (B), a zoomed in example of a cuff-induced curve transient (C) and apparent curve dependencies between muscles (D), including gastrocnemius medialis (green) and gastrocnemius lateralis (red). Magenta lines can be disregarded.*

The present study confirmed current literature in that most clinically relevant dynamic BOLD effects were found in the hyperemic upslope. The measures characterizing this segment were *the hyperemic upslope*, *the time to peak* and the *time to half peak*. In patients, measurements in soleus frequently provided higher quality curves when compared to those in the gastrocnemius muscle.

DISCUSSION

Clinical relevance

Paper I
In clinical or research scenarios, where CBF (or MTT) parameter maps are compared between the techniques, it is important to be aware that parameters from DCE-CT may be underestimated (or overestimated) in comparison to estimates from DSC-MRI, especially in highly perfused areas. These differences between the techniques have, to the authors knowledge, previously not received much attention in the literature.

The clinically most used perfusion parameter, however, is the rCBV. The findings of paper I in regard to CBV, that this is the parameter least sensitive to the injection duration effect, are likely valid also for rCBV estimates. When CBV is estimated without deconvolution, as in Eq. 20 the integrals of the AIF and the tissue-concentration-time-curve provides some robustness against moderate levels of noise. These benefits of CBV-estimates are likely a part of the explanation to why rCBV-estimates have been successfully adopted in the clinical setting.

Paper II
Paper II showed that the increase in rCBF after shunt-surgery in mecencephalon and pons correlated with disease symptom improvements. This strengthens the hypothesis that these neuroanatomical regions may be involved in the disease symptom and potential reversibility of iNPH. However, no differences were found between any pre-operative perfusion parameters (rCBF, rCBV, MTT) between patients and controls, nor any differences for any perfusion parameters when all post-operative patients were compared to controls. Thus, indicating that intragroup and intersubject variabilities were relatively high, with large overlaps between groups.

ADC estimates were found lower in preoperative patients when compared to controls, and estimates decreased further postoperatively. In all individual ROIs except the posterior ROIs in mecencephalon and pons, ADC was reduced postoperatively. However, these changes did not correlate with symptom improvements.

The ADC is a coarse measure of diffusion to start with as all signal effects that contribute to signal decreases during the diffusion weighting will be included in this single-parameter representation. The currently used diffusion weighting is less specific from a measurement perspective, due to the inclusion of the b=0 s/mm^2. This makes the ADC estimate sensitive to intravoxel incoherent motion, the contribution of the microvascular blood compartment to the measured diffusion signal decrease. The fact that differences between subject groups pre- and postoperatively could be detected is encouraging for future developments toward the application of more specific dMRI techniques to this patient cohort[118].

Paper III

Paper III was based on a small cohort of healthy subjects to minimize the possibility of cofounding factors. This paper was focused on the acquisition protocol and how to apply the arterial occlusion in order to obtain strong and reproducible BOLD-curve measures. The results show that the duration of the occlusion indeed can affect the hyperemic response and derived measures. Hence, as the technique is developed further towards clinical adoption, and as standardization efforts are made to optimize image acquisition protocols, the arterial occlusion duration is a parameter that should be taken into regard.

Since the subjects included in this study were young and healthy, the effect of the arterial occlusion duration on elderly healthy subjects, as well as PAD patients should be included in future standardization efforts. It is reasonable to expect similar or slightly smaller differences in an elderly population. Optimally, cuffing should be made sufficiently long for all potential subject groups, but as short as possible to minimize MRI scan duration.

Paper IV

One of the interesting findings in this study was the relatively frequent acquisitions of unexpected curve traits in the gastrocnemius muscles. While the reason for these deviating curves has not fully been established, the possibility that the cause is related to the leg placement in the scanner or differences in the padding of patients and healthy subjects cannot be entirely excluded. From a clinical perspective it is important to understand these causes in order to maximize repeatability of the technique under experimental conditions.

A second finding was that while data from the gastrocnemius ROI often was deemed unusable, soleus curves were often acceptable. Based on the derived

measures from the soleus muscle, patients and age-matched controls were easily separated based on the hyperemic upslope measures. If the data in soleus continues to provide more reliable measurements, its recommended use over other muscles could be considered.

Quantitative vs. relative estimates of perfusion

Paper I

This work showed that CBF-estimates in DCE-CT perfusion, which occasionally is used in parallel to DSC-MRI, depends on the injection duration. Longer injection durations can lead to estimate bias in CBF and MTT in highly perfused regions, while CBV estimates were proven to be robust against longer injection durations. These findings will hold true also when considering relative CBF estimates, given that the reference region used during normalization is not a highly perfused area.

The oSVD deconvolution algorithm used in the evaluation of paper I is known to underestimate perfusion at high levels of CBF. Can the increased difficulty to estimate highly perfused regions at longer injection durations be dismissed as a property of the deconvolution technique? While each deconvolution technique has different qualities, it is believed that the results with increased bias and variability reflects the increased difficulty of solving an inverse problem when the solution has been encoded onto longer arrays. It is a possibility, however, that more recently developed deconvolution algorithms perform better than oSVD-deconvolution on these tasks.

Paper II

The surgical intervention where ventriculo-peritoneal shunts were installed caused severe susceptibility artifacts in the postoperative GE-EPI-based perfusion raw data. While care was taken to exclude these areas from analysis, we cannot entirely rule out the influence of susceptibility induced effects on post-operative estimates. Furthermore, it was found that occasionally sessions were terminated near the ending of the first bolus-passage. AIF-partial volume correction schemes based on tail-scaling (that do not require any extra acquired data), could thus not be leveraged for a portion of the subjects. To process all subjects equally, relative estimates of perfusion were derived.

During data-processing, special care was taken to exclude vessels and CSF from the ROIs prior to the averaging of signal-time curves. This was done first by use of an automated clustering, which during quality control was improved by a manual trimming of the ROI by the radiologist if necessary.

Paper III and IV

In paper III and IV BOLD imaging was applied to assess perfusion in peripheral calf muscle. While quantitative estimates of T_2^* are derived from raw images, no quantitative estimates of peripheral perfusion can be derived with the technique to date. Repeatability was evaluated in paper III and found excellent in regard to operator-related variations. Inter- and intra-session variability was found relatively low.

The arterial inflow to the muscles appears to have substantial influence over the shape of the T_2^*-time curve. While large vessel properties are highly relevant to measure for the patient group, the ability to capture more specific properties, that reflect properties of the capillary bed and oxygen metabolism is highly relevant from a clinical perspective. Theory describing changes to vascular volume fractions during the BOLD MRI acquisition, is warranted in order to enable estimation of quantitative perfusion parameters with the technique.

For the evaluation of PAD, MRI techniques DCE-MRI, ASL, IVIM and crCEST appear to be the most interesting to compare against cuff-based BOLD. These are techniques that provide quantitative measures of perfusion or reflect metabolic function, each with its own level of measurement accuracy and precision. Current cuff-based BOLD analysis does not provide quantitative measures of perfusion. However, it can still reflect perfusion properties and derived measures may hold relevant information to assessments of PAD. Hence, it remains to be seen which of these techniques provide the best basis for clinical decision-making.

CONCLUSION AND FUTURE PERSPECTIVES

What has this thesis contributed toward the primary and secondary aims of this thesis? In regard to the primary aim, to advance the knowledge regarding certain aspects of acquisition and measurement in perfusion imaging, paper I and III, are the primary articles to consider. To conclude, we now know that acquisition parameters such as the duration of the contrast agent injection in DSC-MRI and the cuffing duration in peripheral muscle BOLD imaging can influence the measures derived by each technique.

In regard to the secondary aim of this thesis, to apply these techniques in clinically relevant patient cohorts, paper II and IV, are the primary articles to consider. Results in paper II, show that the mesencephalon and pons are likely involved in the iNPH disease and its potential reversibility, as reflected by a post-operative increase in rCBF that follows the rate of clinical improvement in shunt-responders. Future studies on larger cohorts are needed to validate the results of previous exploratory, small-cohort studies, such as paper II. In parallel, studies exploring other MR-contrast mechanisms and their potential to probe neurophysiology, relevant to the disease, are motivated. Techniques that combine BOLD and ASL acquisition with gas paradigms can potentially provide measures of oxygen metabolism. Animal studies on the glymphatic system show its potential involvement in iNPH and the use of contrast enhanced T1-weighted imaging may help enlighten these mechanisms further in humans[119]. The potential to sensitize microstructural tissue properties of the brain via advanced diffusion MRI techniques also appears promising[118].

In paper IV, cuff-based peripheral muscle BOLD imaging was applied to a small cohort of PAD patients and two control groups. Paper IV showed for the first time that the T_2^*-time curves of patients can be difficult to interpret and can be associated with unexpected curve traits that do not always align with the most basic expectations on the response of the muscle to the cuffing sequence. It was also shown that these effects were more frequent in gastrocnemius rather than soleus muscles. To seek the causes of the observed deviating curve traits, whether they have scan-technical or physiological explanations, requires further studies.

Paper IV also confirmed previous results showing that the technique can separate patients from age-matched controls based on the soleus muscle even when data from the gastrocnemius ROI of several patients (n=10, 53%) had to be disregarded due to low quality. The most discriminative perfusion related measures were related to the upslope of the hyperemic response. Future work should be targeted on studying the BOLD effect during this segment of the cuffing paradigm in more detail by e.g. using pixel-based rather than ROI-based analysis, enabling spatial intensity and pattern variations to be determined. Such detailed analysis may reveal regional changes associated to pathology but also enable separations between macroscopical tissue structures into e.g. fat, blood vessels and muscle tissue. From a clinical perspective, current PAD image diagnosis is mainly performed via angiographic imaging techniques, by studying the vessel tree. Also, measures of ankle brachial index can be used but in similarity to angiography, it produces a coarse measure of the macrovascular state. Paper IV shows that similar group-wise separations as ABI can be achieved with peripheral muscle BOLD imaging. Hopefully, more detailed analysis of the BOLD MR images can contribute with new information that can strengthen the diagnosis and increase the prediction of response to intervention on an individual level. As the lack of a gold-standard reference measure of microvascular tissue function may become challenging, intervention studies could be an attractive alternative to enable the evaluation of the clinical use of the technique.

Shifting perspective from individual studies of this thesis to the field of perfusion imaging and the techniques used, the two main techniques used can indeed be placed at opposite ends of a hypothetical technical maturity-scale. The challenges associated with quantitative perfusion estimation in DSC-MRI are at this stage well documented and addressed, in most cases by several alternative approaches. While the possibilities and potential limitations of peripheral muscle BOLD imaging are still being explored.

Improving the acquisition scheme in DSC-MRI has been suggested in the literature, such as combining gradient- and spin-echo acquisitions[120–123] and multiple echo-times to more efficiently separate micro and macrovascular[59] signal contributions and provide leakage corrections[124]. However, while developments toward richer and richer data appears reasonable from a technical perspective, in the clinic, contrast-agent based techniques are competing against alternatives that do not require the hassle of an intra-venous injection during the scan-session. The current precautions against the use of gadolinium-based contrast agents and the recent developments on the topic of

contrast agent deposits[31] adds to the interest of exploring alternative MRI techniques. Adding more complexity to the technique at this stage could become detrimental to a continued widespread clinical adoption, why balancing technical gains with practicality appears necessary. The fact is that correction techniques that require additional bolus injections or altered scan sequences have not reached clinical adoption, and in the clinic, rCBV-estimates remains the most common perfusion estimate of DSC-MRI.

The challenge of standardization of functional imaging techniques, such as DSC-MRI, has recently been recognized in the research community. Recent years has seen the rise of open-research initiatives and the relatively new interest toward reproducible research. Standardization of post-processing software and supporting the benchmarking of alternative software solutions on common data sets are topics within the scope of the open science initiative for perfusion imaging (OSIPI)[125]. The relatively new OSIPI code repository and testing framework[126] is a platform initiated by the perfusion study group of the ISMRM, where world-wide collaborative efforts on these topics are currently taking place.

The research field of perfusion MRI spans many categories of topics. These include, but are not limited to, 1) MRI physics and scan sequence optimization, 2) experimental factors to enhance the perfusion-related signal contrast, 3) pre-processing and correction techniques, 4) modelling theory, 5) the analysis of data to produce estimates of perfusion, and 6) post-processing such as scaling, normalization, and standardization of derived perfusion measures. When considering the combined complexity of this entire measurement apparatus, it becomes clear that research development is driven forward collectively by many. With the pooled efforts of a world-wide research community, a future with the successful clinical adoption of accurate and precise perfusion imaging techniques appears bright and hopeful.

ACKNOWLEDGEMENTS

REFERENCES

1.   Cercignani M, Dowell NG, Tofts PS. *Quantitative MRI of the Brain: Principles of Physical Measurement.*; 2018. https://www.routledge.com/Quantitative-MRI-of-the-Brain-Principles-of-Physical-Measurement-Second/Cercignani-Dowell-Tofts/p/book/9780367781538. Accessed October 15, 2023.

2.   Munoz CJ, Lucas A, Williams AT, Cabrales P. A Review on Microvascular Hemodynamics: The Control of Blood Flow Distribution, and Tissue Oxygenation. 2020. doi:10.1016/j.ccc.2019.12.011

3.   Kessler LG, Barnhart HX, Buckler AJ, et al. The emerging science of quantitative imaging biomarkers terminology and definitions for scientific studies and regulatory submissions. *Stat Methods Med Res*. 2015;24(1):9-26. doi:10.1177/0962280214537333

4.   Betts JG, Desaix P, Johnson E, et al. Anatomy and physiology. OpenStax. *Rice University: Houston, TX, USA*. 2013. https://openstax.org/books/anatomy-and-physiology. Accessed September 15, 2023.

5.   Snyder GK, Sheafor BA. Red Blood Cells: Centerpiece in the Evolution of the Vertebrate Circulatory System. *Integr Comp Biol*. 1999;39(2):189-198. doi:10.1093/ICB/39.2.189

6.   Ivanov KP, Kalinina MK, Levkovich YI. Blood flow velocity in capillaries of brain and muscles and its physiological significance. *Microvasc Res*. 1981;22(2):143-155. doi:10.1016/0026-2862(81)90084-4

7.   Fåhraeus R. THE SUSPENSION STABILITY OF THE BLOOD. *https://doi.org/101152/physrev192992241*. 1929;9(2):241-274. doi:10.1152/PHYSREV.1929.9.2.241

8.   Dickie BR, Ahmed Z, Arvidsson J, et al. A community-endorsed open-source lexicon for contrast agent–based perfusion MRI: A consensus guidelines report from the ISMRM Open Science Initiative for

Perfusion Imaging (OSIPI). *Magn Reson Med*. October 2023. doi:10.1002/MRM.29840

9.   Donahue MJ, Achten E, Cogswell PM, et al. Consensus statement on current and emerging methods for the diagnosis and evaluation of cerebrovascular disease. *Journal of Cerebral Blood Flow & Metabolism*. 2018;38(9):1391-1417. doi:10.1177/0271678X17721830

10.   Pollak AW, Meyer CH, Epstein FH, et al. Arterial Spin Labeling MR Imaging Reproducibly Measures Peak-Exercise Calf Muscle Perfusion: A Study in Patients With Peripheral Arterial Disease and Healthy Volunteers. *JACC Cardiovasc Imaging*. 2012;5(12):1224-1230. doi:10.1016/J.JCMG.2012.03.022

11.   Gutterman DD, Chabowski DS, Kadlec AO, et al. The Human Microcirculation. *Circ Res*. 2016;118(1):157-172. doi:10.1161/CIRCRESAHA.115.305364

12.   Cox JA, Bartlett E, Lee EI. Vascular malformations: A review. *Semin Plast Surg*. 2014;28(2):58-63. doi:10.1055/S-0034-1376263/ID/JR01015-26/BIB

13.   Lugano R, Ramachandran M, Dimberg A. Tumor angiogenesis: causes, consequences, challenges and opportunities. *Cellular and Molecular Life Sciences*. 2020;77(9):1745. doi:10.1007/S00018-019-03351-7

14.   Stapf C, Mohr JP, Pile-Spellman J, Solomon RA, Sacco RL, Connolly ES. Epidemiology and natural history of arteriovenous malformations. *Neurosurg Focus*. 2001;11(5):1-5. doi:10.3171/FOC.2001.11.5.2

15.   Krauss JK, Regel JP, Vach W, Droste DW, Borremans JJ, Mergner T. Vascular risk factors and arteriosclerotic disease in idiopathic normal-pressure hydrocephalus of the elderly. *Stroke*. 1996;27(1):24-29. doi:10.1161/01.STR.27.1.24

16.   Graff-Radford NR, Godersky JC. Idiopathic normal pressure hydrocephalus and systemic hypertension. *Neurology*. 1987;37(5):868-871. doi:10.1212/WNL.37.5.868

17. Jaraj D, Agerskov S, Rabiei K, et al. Vascular factors in suspected normal pressure hydrocephalus: A population-based study. *Neurology*. 2016;86(7):592-599. doi:10.1212/WNL.0000000000002369

18. Ziegelitz D, Arvidsson J, Hellström P, Tullberg M, Wikkelsø C, Starck G. In Patients with Idiopathic Normal Pressure Hydrocephalus Postoperative Cerebral Perfusion Changes Measured by Dynamic Susceptibility Contrast Magnetic Resonance Imaging Correlate with Clinical Improvement. *J Comput Assist Tomogr*. 2015;39(4). doi:10.1097/RCT.0000000000000254

19. Joosten MM, Pai JK, Bertoia ML, et al. Associations Between Conventional Cardiovascular Risk Factors and Risk of Peripheral Artery Disease in Men. *JAMA*. 2012;308(16):1660-1667. doi:10.1001/JAMA.2012.13415

20. Pizzimenti M, Meyer A, Charles AL, et al. Sarcopenia and peripheral arterial disease: a systematic review. *J Cachexia Sarcopenia Muscle*. 2020;11(4):866-886. doi:10.1002/jcsm.12587

21. Wintermark M, Sesay M, Barbier E, et al. Comparative Overview of Brain Perfusion Imaging Techniques. *Stroke*. 2005;36(9). doi:10.1161/01.str.0000177884.72657.8b

22. Novikov DS, Kiselev VG, Jespersen SN. On modeling. *Magn Reson Med*. 2018;79(6):3172-3193. doi:10.1002/mrm.27101

23. Novikov DS, Kiselev VG, Jespersen SN. On modeling. *Magn Reson Med*. 2018;79(6):3172-3193. doi:10.1002/mrm.27101

24. Fieselmann A, Kowarschik M, Ganguly A, Hornegger J, Fahrig R. Deconvolution-Based CT and MR Brain Perfusion Measurement: Theoretical Model Revisited and Practical Implementation Details. *Int J Biomed Imaging*. August 2011. doi:0.1155/2011/467563

25. Wirestam R. Using contrast agents to obtain maps of regional perfusion and capillary wall permeability. *Imaging Med*. 2012;4(4):423-442. doi:10.2217/iim.12.24

26. Knutsson L, Stahlberg F, Wirestam R. Absolute quantification of perfusion using dynamic susceptibility contrast MRI: pitfalls and

possibilities. *Magn Reson Mater Phy*. 2010;23(1):1-21. doi:10.1007/s10334-009-0190-2

27. Ahlgren A. Methodological improvements in quantitative MRI: Perfusion estimation and partial volume considerations. January 2017.

28. Lind E. MRI Perfusion Measurements using Magnetic Susceptibility Effects: Calibration Approaches and Contrast Agent Quantification. 2019.

29. Rosen BR, Belliveau JW, Vevea JM, Brady TJ. Perfusion imaging with NMR contrast agents. *Magn Reson Med*. 1990;14(2):249-265. doi:10.1002/MRM.1910140211

30. Barbier EL, Lamalle L, Décorps M. Methodology of brain perfusion imaging. *Journal of Magnetic Resonance Imaging*. 2001;13(4):496-520. http://onlinelibrary.wiley.com/doi/10.1002/jmri.1073/abstract.

31. Mathur M, Jones JR, Weinreb JC. Gadolinium deposition and nephrogenic systemic fibrosis: A radiologist's primer. *Radiographics*. 2020;40(1):153-162. doi:10.1148/RG.2020190110/ASSET/IMAGES/LARGE/RG.2020190110.TBL4.JPEG

32. Meier P, Zierler KL. On the theory of the indicator-dilution method for measurement of blood flow and volume. *J Appl Physiol*. 1954;6(12):731-744. doi:10.1152/jappl.1954.6.12.731

33. Zierler KL. Equations for measuring blood flow by external monitoring of radioisotopes. *Circ Res*. 1965;16(4):309-321.

34. Axel L. Cerebral blood flow determination by rapid-sequence computed tomography: theoretical analysis. *Radiology*. 1980;137(3):679-686.

35. Mouridsen K, Christensen S, Gyldensted L, Ostergaard L. Automatic selection of arterial input function using cluster analysis. *Magn Reson Med*. 2006;55(3):524-531. doi:10.1002/mrm.20759

36. Peruzzo D, Bertoldo A, Zanderigo F, Cobelli C. Automatic selection of arterial input function on dynamic contrast-enhanced MR images.

Comput Methods Programs Biomed. 2011;104. doi:10.1016/j.cmpb.2011.02.012

37.   Rempp KA, Brix G, Wenz F, Becker CR, Gückel F, Lorenz WJ. Quantification of regional cerebral blood flow and volume with dynamic susceptibility contrast-enhanced MR imaging. *Radiology*. 1994;193(3):637-641.

38.   Fieselmann A, Kowarschik M, Ganguly A, Hornegger J, Fahrig R. Deconvolution-Based CT and MR Brain Perfusion Measurement: Theoretical Model Revisited and Practical Implementation Details. Erlandsson K, ed. *Int J Biomed Imaging*. 2011;2011:467563. doi:10.1155/2011/467563

39.   Stewart GN. Researches on the circulation time in organs and on the influences which affect it. *J Physiol*. 1893;15(7):1-2.

40.   Perthen JE, Calamante F, Gadian DG, Connelly A. Is quantification of bolus tracking MRI reliable without deconvolution? *Magn Reson Med*. 2002;47(1):61-67.

41.   Meijs M, Christensen S, Lansberg MG, Albers GW, Calamante F. Analysis of perfusion MRI in stroke: To deconvolve, or not to deconvolve. *Magn Reson Med*. 2015. doi:10.1002/mrm.26024

42.   Weisskoff RM, Chesler D, Boxerman JL, Rosen BR. Pitfalls in MR measurement of tissue blood flow with intravascular tracers: which mean transit time? *Magn Reson Med*. 1993;29(4):553-558. doi:10.1002/MRM.1910290420

43.   Østergaard L, Weisskoff RM, Chesler DA, Gyldensted G, Rosen BR. High resolution measurement of cerebral blood flow using intravascular tracer bolus passages. Part I: Mathematical approach and statistical analysis. *Magn Reson Med*. 1996;36(5):715-725. doi:10.1002/MRM.1910360510

44.   Wu O, Ostergaard L, Weisskoff RM, Benner T, Rosen BR, Sorensen AG. Tracer arrival timing-insensitive technique for estimating flow in MR perfusion-weighted imaging using singular value decomposition with a block-circulant deconvolution matrix. *Magn Reson Med*. 2003;50(1):164-174. doi:10.1002/mrm.10522

45. Calamante F, Gadian DG, Connelly A. Quantification of bolus-tracking MRI: Improved characterization of the tissue residue function using Tikhonov regularization. *Magn Reson Med.* 2003;50(6):1237-1247. doi:10.1002/mrm.10643

46. Chen JJ, Smith MR, Frayne R. Advantages of frequency-domain modeling in dynamic-susceptibility contrast magnetic resonance cerebral blood flow quantification. *Magn Reson Med*. 2005;53(3):700-707.

47. Mouridsen K, Friston K, Hjort N, Gyldensted L, Østergaard L, Kiebel S. Bayesian estimation of cerebral perfusion using a physiological model of microvasculature. *Neuroimage*. 2006;33(2):570-579.

48. Mehndiratta A, MacIntosh BJ, Crane DE, Payne SJ, Chappell MA. A control point interpolation method for the non-parametric quantification of cerebral haemodynamics from dynamic susceptibility contrast MRI. *Neuroimage*. 2013;64:560-570.

49. Zanderigo F, Bertoldo A, Pillonetto G, Cobelli C. Nonlinear stochastic regularization to characterize tissue residue function in bolus-tracking MRI: assessment and comparison with SVD, block-circulant SVD, and Tikhonov. *Biomedical Engineering, IEEE Transactions on.* 2009;56(5):1287-1297.

50. Boutelier T, Kudo K, Pautot F, Sasaki M. Bayesian hemodynamic parameter estimation by bolus tracking perfusion weighted imaging. *IEEE Trans Med Imaging*. 2012;31(7):1381-1395. doi:10.1109/tmi.2012.2189890

51. Pizzolato M, Boutelier T, Deriche R. Perfusion deconvolution in DSC-MRI with dispersion-compliant bases. *Med Image Anal*. 2017;36:197-215. doi:http://dx.doi.org/10.1016/j.media.2016.12.001

52. Chakwizira A, Ahlgren A, Knutsson L, Wirestam R. Non-parametric deconvolution using Bézier curves for quantification of cerebral perfusion in dynamic susceptibility contrast MRI. *MAGMA*. January 2022. doi:10.1007/S10334-021-00995-0

53. Andersen IK, Szymkowiak A, Rasmussen CE, et al. Perfusion quantification using Gaussian process deconvolution. *Magn Reson Med*. 2002;48(2):351-361. doi:10.1002/MRM.10213

54. Gobbel GT, Fike JR. A deconvolution method for evaluating indicator-dilution curves. *Phys Med Biol*. 1994;39(11):1833.

55. Peruzzo D, Castellaro M, Pillonetto G, Bertoldo A. Stable spline deconvolution for dynamic susceptibility contrast MRI. *Magn Reson Med*. 2017;78(5):1801-1811. doi:10.1002/mrm.26582

56. Giacalone M, Frindel C, Robini M, Cervenansky F, Grenier E, Rousseau D. Robustness of spatio-temporal regularization in perfusion MRI deconvolution: An application to acute ischemic stroke. *Magn Reson Med*. 2017;78(5):1981-1990. doi:10.1002/MRM.26573

57. Sourbron S, Dujardin M, Makkat S, Luypaert R. Pixel-by-pixel deconvolution of bolus-tracking data: Optimization and implementation. *Phys Med Biol*. 2007;52(2):429-447. doi:10.1088/0031-9155/52/2/009

58. Wirestam R, Ståhlberg F. Wavelet-based noise reduction for improved deconvolution of time-series data in dynamic susceptibility-contrast MRI. *Magnetic Resonance Materials in Physics, Biology and Medicine*. 2005;18(3):113-118. doi:10.1007/s10334-005-0102-z

59. Chappell MA, Mehndiratta A, Calamante F. Correcting for large vessel contamination in dynamic susceptibility contrast perfusion MRI by extension to a physiological model of the vasculature. *Magn Reson Med*. 2015;74(1):280-290. doi:10.1002/mrm.25390

60. Kroll K, Wilke N, Jerosch-Herold M, et al. Modeling regional myocardial flows from residue functions of an intravascular indicator. *Am J Physiol Heart Circ Physiol*. 1996;271(4):H1643 LP-H1655. http://ajpheart.physiology.org/content/271/4/H1643.abstract.

61. Ostergaard L, Chesler DA, Weisskoff RM, Sorensen AG, Rosen BR. Modeling Cerebral Blood Flow and Flow Heterogeneity From Magnetic Resonance Residue Data. *J Cereb Blood Flow Metab*. 1999;19(6):690-699. http://dx.doi.org/10.1097/00004647-199906000-00013.

62. Sourbron S, Luypaert R, Morhard D, Seelos K, Reiser M, Peller M. Deconvolution of bolus-tracking data: a comparison of discretization methods. *Phys Med Biol*. 2007;52(22):6761. http://stacks.iop.org/0031-9155/52/i=22/a=014.

63. Mouridsen K, Hansen MB, Østergaard L, Jespersen SN. Reliable estimation of capillary transit time distributions using DSC-MRI. *Journal of Cerebral Blood Flow & Metabolism*. 2014;34(9):1511-1521.

64. Willats L, Calamante F. The 39 steps: evading error and deciphering the secrets for accurate dynamic susceptibility contrast MRI. *NMR Biomed*. 2013;26(8):913-931. doi:10.1002/nbm.2833

65. Calamante F. Arterial input function in perfusion MRI: a comprehensive review. *Prog Nucl Magn Reson Spectrosc*. 2013;74:1-32.

66. Calamante F. Bolus dispersion issues related to the quantification of perfusion MRI data. *J Magn Reson Imaging*. 2005;22(6):718-722. doi:10.1002/jmri.20454

67. Calamante F, Gadian DG, Connelly A. Delay and dispersion effects in dynamic susceptibility contrast MRI: Simulations using singular value decomposition. *Magn Reson Med*. 2000;44(3):466-473. doi:10.1002/1522-2594(200009)44:3<466::AID-MRM18>3.0.CO;2-M

68. Willats L, Connelly A, Calamante F. Minimising the effects of bolus dispersion in bolus-tracking MRI. *NMR Biomed*. 2008;21(10):1126-1137. doi:10.1002/nbm.1290

69. Calamante F, Mørup M, Hansen LK. Defining a local arterial input function for perfusion MRI using independent component analysis. *Magn Reson Med*. 2004;52(4):789-797. doi:10.1002/mrm.20227

70. Willats L, Christensen S, Ma HK, Donnan GA, Connelly A, Calamante F. Validating a local Arterial Input Function method for improved perfusion quantification in stroke. *Journal of Cerebral Blood Flow & Metabolism*. 2011;31(10):2189-2198. doi:10.1038/jcbfm.2011.78

71. Knutsson L, Larsson EM, Thilmann O, Ståhlberg F, Wirestam R. Calculation of cerebral perfusion parameters using regional arterial input functions identified by factor analysis. *Journal of Magnetic Resonance Imaging*. 2006;23(4):444-453. doi:10.1002/jmri.20535

72. Lee JJ, Bretthorst GL, Derdeyn CP, et al. Dynamic susceptibility contrast MRI with localized arterial input functions. *Magn Reson Med*. 2010;63(5):1305-1314. doi:10.1002/mrm.22338

73. Mehndiratta A, Calamante F, Macintosh BJ, Crane DE, Payne SJ, Chappell MA. Modeling and correction of bolus dispersion effects in dynamic susceptibility contrast MRI. *Magn Reson Med*. 2014;72(6):1762-1774. doi:10.1002/mrm.25077

74. Kjølby BF, Mikkelsen IK, Pedersen M, Østergaard L, Kiselev VG. Analysis of partial volume effects on arterial input functions using gradient echo: A simulation study. *Magn Reson Med*. 2009;61(6):1300-1309. doi:10.1002/mrm.21849

75. Kellner E, Mader I, Mix M, et al. Arterial input function measurements for bolus tracking perfusion imaging in the brain. *Magn Reson Med*. 2013;69(3):771-780. doi:10.1002/mrm.24319

76. Van Osch MJP, Vonken EJPA, Bakker CJG, Viergever MA. Correcting partial volume artifacts of the arterial input function in quantitative cerebral perfusion MRI. *Magn Reson Med*. 2001;45(3):477-485. doi:10.1002/1522-2594(200103)45:3<477::AID-MRM1063>3.0.CO;2-4

77. Bjornerud A, Emblem KE. A fully automated method for quantitative cerebral hemodynamic analysis using DSC-MRI. *J Cereb Blood Flow Metab*. 2010;30(5):1066-1078. doi:10.1038/jcbfm.2010.4

78. Knutsson L, Lindgren E, Ahlgren A, et al. Dynamic susceptibility contrast MRI with a prebolus contrast agent administration design for improved absolute quantification of perfusion. *Magn Reson Med*. 2014;72(4):996-1006. doi:10.1002/mrm.25006

79. Hansen MB, Tietze A, Kalpathy-Cramer J, et al. Reliable estimation of microvascular flow patterns in patients with disrupted blood-brain

barrier using dynamic susceptibility contrast MRI. *Journal of Magnetic Resonance Imaging*. 2017;46(2):537-549. doi:10.1002/jmri.25549

80. Boxerman JL, Schmainda KM, Weisskoff RM. Relative Cerebral Blood Volume Maps Corrected for Contrast Agent Extravasation Significantly Correlate with Glioma Tumor Grade, Whereas Uncorrected Maps Do Not. *AJNR Am J Neuroradiol*. 2006;27(4):859. /pmc/articles/PMC8134002/. Accessed October 4, 2023.

81. van Osch MJP, Vonken E jan PA, Wu O, Viergever MA, van der Grond J, Bakker CJG. Model of the human vasculature for studying the influence of contrast injection speed on cerebral perfusion MRI. *Magn Reson Med*. 2003;50(3):614-622. doi:10.1002/mrm.10567

82. Caroca S, Villagran D, Chabert S. Four functional magnetic resonance imaging techniques for skeletal muscle exploration, a systematic review. *Eur J Radiol*. 2021;144. doi:10.1016/J.EJRAD.2021.109995

83. Mathew RC, Kramer CM. Recent advances in magnetic resonance imaging for peripheral artery disease. *Vasc Med*. 2018;23(2):143. doi:10.1177/1358863X18754694

84. Versluis B, Dremmen MHG, Nelemans PJ, Wildberger JE, Schurink GW. Dynamic Contrast-Enhanced MRI Assessment of Hyperemic Fractional Microvascular Blood Plasma Volume in Peripheral Arterial Disease: Initial Findings. *PLoS One*. 2012;7(5):37756. doi:10.1371/journal.pone.0037756

85. Tang H, Yu L, Suo S, et al. Evaluation of skeletal muscle perfusion changes in patients with peripheral artery disease before and after percutaneous transluminal angioplasty using multiparametric MR imaging. *Magn Reson Imaging*. 2022;93:157-162. doi:10.1016/J.MRI.2022.08.001

86. Isbell DC, Berr SS, Toledano AY, et al. Delayed Calf Muscle Phosphocreatine Recovery After Exercise Identifies Peripheral Arterial Disease. 2006. doi:10.1016/j.jacc.2005.12.069

87. Kogan F, Haris M, Debrosse C, et al. In vivo chemical exchange saturation transfer imaging of creatine (CrCEST) in skeletal muscle at

3T. *Journal of Magnetic Resonance Imaging*. 2014;40(3):596-602. doi:10.1002/JMRI.24412

88.   Toussaint JF, Kwong KK, M'Kparu F, Weisskoff RM, LaRaia PJ, Kantor HL. Perfusion changes in human skeletal muscle during reactive hyperemia measured by echo-planar imaging. *Magn Reson Med*. 1996;35(1):62-69. doi:10.1002/MRM.1910350109

89.   Kim SG, Ogawa S. Biophysical and physiological origins of blood oxygenation level-dependent fMRI signals. *Journal of Cerebral Blood Flow & Metabolism*. 2012;32:1188-1206. doi:10.1038/jcbfm.2012.23

90.   Ogawa S, Lee TM, Kay AR, Tank DW. Brain magnetic resonance imaging with contrast dependent on blood oxygenation. *Proc Natl Acad Sci U S A*. 1990;87(24):9868-9872. doi:10.1073/PNAS.87.24.9868

91.   Buxton RB. Dynamic Models of BOLD Contrast. 2012. doi:10.1016/j.neuroimage.2012.01.012

92.   Griffeth VEM, Buxton RB. A theoretical framework for estimating cerebral oxygen metabolism changes using the calibrated-BOLD method: modeling the effects of blood volume distribution, hematocrit, oxygen extraction fraction, and tissue signal properties on the BOLD signal. *Neuroimage*. 2011;58(1):198-212. doi:10.1016/j.neuroimage.2011.05.077

93.   Lee SP, Duong TQ, Yang G, Iadecola C, Kim SG. Relative changes of cerebral arterial and venous blood volumes during increased cerebral blood flow: Implications for BOLD fMRI. *Magn Reson Med*. 2001;45(5):791-800. doi:10.1002/MRM.1107

94.   Ogawa S, Menon RS, Tank DW, et al. Functional brain mapping by blood oxygenation level-dependent contrast magnetic resonance imaging. A comparison of signal characteristics with a biophysical model. *Biophys J*. 1993;64(3):803-812. doi:10.1016/S0006-3495(93)81441-3

95.   Damon BM, Gore JC. Physiological basis of muscle functional MRI: Predictions using a computer model. *J Appl Physiol*. 2005;98(1):264-273. doi:10.1152/japplphysiol.00369.2004

96.   Kim T, Hendrich KS, Masamoto K, Kim SG. Arterial versus total blood volume changes during neural activity-induced cerebral blood flow change: Implication for BOLD fMRI. *Journal of Cerebral Blood Flow and Metabolism*. 2007;27(6):1235-1247. doi:10.1038/sj.jcbfm.9600429

97.   Ledermann HP, Schulte AC, Heidecker HG, et al. Blood oxygenation level-dependent magnetic resonance imaging of the skeletal muscle in patients with peripheral arterial occlusive disease. *Circulation*. 2006;113(25):2929-2935. doi:10.1161/CIRCULATIONAHA.105.605717

98.   Li Z, Muller MD, Wang J, et al. Dynamic characteristics of T2*-weighted signal in calf muscles of peripheral artery disease during low-intensity exercise. *Journal of Magnetic Resonance Imaging*. 2017;46(1):40-48. doi:10.1002/jmri.25532

99.   Englund EK, Langham MC, Ratcliffe SJ, et al. Multiparametric assessment of vascular function in peripheral artery disease: Dynamic measurement of skeletal muscle perfusion, blood-oxygen-level dependent signal, and venous oxygen saturation. *Circ Cardiovasc Imaging*. 2015;8(4):1-10. doi:10.1161/CIRCIMAGING.114.002673

100.   Bakermans AJ, Wessel CH, Zheng KH, Groot PFC, Stroes ESG, Nederveen AJ. Dynamic magnetic resonance measurements of calf muscle oxygenation and energy metabolism in peripheral artery disease. *Journal of Magnetic Resonance Imaging*. 2020;51(1):98-107. doi:10.1002/jmri.26841

101.   Törngren K, Eriksson S, Arvidsson J, et al. A reperfusion BOLD-MRI tissue perfusion protocol reliably differentiate patients with peripheral arterial occlusive disease from healthy controls. *J Clin Med*. 2021;10(16):28-29. doi:10.3390/jcm10163643

102.   Bajwa A, Wesolowski R, Patel A, et al. Blood Oxygenation Level-Dependent CMR-Derived Measures in Critical Limb Ischemia and Changes with Revascularization. *J Am Coll Cardiol*. 2016;67(4):420-431. doi:10.1016/j.jacc.2015.10.085

103.   Slade JM, Towse TF, Gossain V V., Meyer RA. Peripheral microvascular response to muscle contraction is unaltered by early

diabetes but decreases with age. *J Appl Physiol*. 2011;111(5):1361-1371. doi:10.1152/japplphysiol.00009.2011

104.   Partovi S, Schulte AC, Aschwanden M, et al. Impaired skeletal muscle microcirculation in systemic sclerosis. *Arthritis Res Ther*. 2012;14(5). doi:10.1186/ar4047

105.   Huegli RW, Aschwanden M, Jacob AL. Effects of percutaneous transluminal angioplasty on muscle BOLD-MRI in patients with peripheral arterial occlusive disease : preliminary results. 2009:509-515. doi:10.1007/s00330-008-1168-6

106.   Steneberg P, Lindahl E, Dahl U, et al. PAN-AMPK activator O304 improves glucose homeostasis and microvascular perfusion in mice and type 2 diabetes patients. *JCI Insight*. 2018;3(12). doi:10.1172/JCI.INSIGHT.99114

107.   Partovi S, Schulte AC, Jacobi B, et al. Blood oxygenation level-dependent (BOLD) MRI of human skeletal muscle at 1.5 and 3 T. *Journal of Magnetic Resonance Imaging*. 2012;35(5):1227-1232. doi:10.1002/JMRI.23583

108.   Jacobi B, Bongartz G, Partovi S, et al. Skeletal Muscle BOLD MRI : From Underlying Physiological Concepts to Its Usefulness in Clinical Conditions. 2012;1265:1253-1265. doi:10.1002/jmri.23536

109.   Suo S, Tang H, Lu Q, et al. Blood oxygenation level-dependent cardiovascular magnetic resonance of the skeletal muscle in healthy adults: Different paradigms for provoking signal alterations. *Magn Reson Med*. 2021;85(3):1590-1601. doi:10.1002/MRM.28495

110.   Stacy MR, Caracciolo CM, Qiu M, et al. Comparison of regional skeletal muscle tissue oxygenation in college athletes and sedentary control subjects using quantitative BOLD MR imaging. *Physiol Rep*. 2016;4(16). doi:10.14814/phy2.12903

111.   Partovi S, Schulte AC, Staub D, et al. Correlation of skeletal muscle blood oxygenation level-dependent MRI and skin laser doppler flowmetry in patients with systemic sclerosis. *Journal of Magnetic Resonance Imaging*. 2014;40(6):1408-1413. doi:10.1002/JMRI.24503

112. Versluis B, Backes WH, van Eupen MGA, et al. Magnetic Resonance Imaging in Peripheral Arterial Disease. *Invest Radiol*. 2011;46(1):11-24. doi:10.1097/rli.0b013e3181f2bfb8

113. Arvidsson J, Eriksson S, Johansson E, Lagerstrand K. Arterial occlusion duration affects the cuff-induced hyperemic response in skeletal muscle BOLD perfusion imaging as shown in young healthy subjects. *Magnetic Resonance Materials in Physics, Biology and Medicine*. June 2023:1-14. doi:10.1007/S10334-023-01105-Y/TABLES/4

114. Englund EK, Langham MC, Li C, et al. Combined measurement of perfusion, venous oxygen saturation, and skeletal muscle T 2 * during reactive hyperemia in the leg. 2013. doi:10.1186/1532-429X-15-70

115. Posse S, Wiese S, Gembris D, et al. Enhancement of BOLD-contrast sensitivity by single-shot multi-echo functional MR imaging. *Magn Reson Med*. 1999;42(1):87-97. doi:10.1002/(sici)1522-2594(199907)42:1<87::aid-mrm13>3.0.co;2-o

116. Schewzow K, Andreas M, Moser E, Wolzt M, Schmid AI. Automatic model-based analysis of skeletal muscle BOLD-MRI in reactive hyperemia. *Journal of Magnetic Resonance Imaging*. 2013;38(4):963-969. doi:10.1002/JMRI.23919

117. Agerskov S, 1 ID, Arvidsson J, et al. MRI diffusion and perfusion alterations in the mesencephalon and pons as markers of disease and symptom reversibility in idiopathic normal pressure hydrocephalus. Burger MC, ed. *PLoS One*. 2020;15(10):e0240327. doi:10.1371/journal.pone.0240327

118. Topgaard D. Multidimensional diffusion MRI. *Journal of Magnetic Resonance*. 2017;275:98-113. doi:10.1016/J.JMR.2016.12.007

119. Ringstad G, Vatnehol SAS, Eide PK. Glymphatic MRI in idiopathic normal pressure hydrocephalus. *Brain*. 2017;140(10):2691-2705. doi:10.1093/brain/awx191

120. Quarles CC, Bell LC, Stokes AM. Imaging vascular and hemodynamic features of the brain using dynamic susceptibility contrast and dynamic

contrast enhanced MRI. *Neuroimage*. 2019;187:32-55. doi:10.1016/J.NEUROIMAGE.2018.04.069

121. Stokes AM, Skinner JT, Quarles CC. Assessment of a combined spin- and gradient-echo (SAGE) DSC-MRI method for preclinical neuroimaging. *Magn Reson Imaging*. 2014;32(10):1181-1190. doi:10.1016/j.mri.2014.08.027

122. Bjornerud A, Sorensen AG, Mouridsen K, Emblem KE. T1- and T2*-dominant extravasation correction in DSC-MRI: Part I—theoretical considerations and implications for assessment of tumor hemodynamic properties. *Journal of Cerebral Blood Flow & Metabolism*. 2011;31(10):2041-2053. doi:10.1038/jcbfm.2011.52

123. Sourbron S, Heilmann M, Biffar A, et al. Bolus-Tracking MRI with a Simultaneous T 1 -and T * 2 -Measurement. *Magn Reson Med*. 2009;62:672-681. doi:10.1002/mrm.22042

124. Stokes AM, Semmineh N, Quarles CC. Validation of a T1 and T2* leakage correction method based on multiecho dynamic susceptibility contrast MRI using MION as a reference standard. *Magn Reson Med*. 2016;76(2):613-625. doi:10.1002/mrm.25906

125. Bell LC, Suzuki Y, van Houdt PJ, Sourbron S, Mutsaerts HJMM. The road to the ISMRM OSIPI: A community-led initiative for reproducible perfusion MRI. *Magn Reson Med*. 2023. doi:10.1002/MRM.29736

126. van Houdt PJ, Ragunathan S, Berks M, et al. Contrast-agent-based perfusion MRI code repository and testing framework: ISMRM Open Science Initiative for Perfusion Imaging (OSIPI). *Magn Reson Med*. 2023. doi:10.1002/MRM.29826